PLEASE CITE THIS ARTICLE AS DOI: 10.1063/5.0141889

Accepted to Phys. Fluids 10.1063/5.0141889

Underwater oscillations of rigid plates with H-shaped cross sections: an experimental study to explore their flow physics

Burak Gulsacan and Matteo Aureli^{a)}
Mechanical Engineering Department
University of Nevada, Reno
1664 N. Virginia Street. Reno. Nevada 89557

In this work, we present a comprehensive experimental study on the problem of harmonic oscillations of rigid plates with H-shaped cross sections submerged in a quiescent, Newtonian, incompressible, viscous fluid environment. Motivated by recent results on minimization of hydrodynamic damping for transversely oscillating flat plates, we conduct a detailed qualitative and quantitative experimental investigation of the flow physics created by the presence of the flanges, that is, the vertical segments in the plate cross section. Specifically, the main goal is to elucidate the effect of flange size on various aspects of fluid-structure interaction, by primarily investigating the dynamics of vortex shedding and convection. We perform particle image velocimetry (PIV) experiments over a broad range of oscillation amplitudes, frequencies, and flange size to width ratios by leveraging the identification of pathlines, vortex shedding and dynamics, distinctive hydrodynamic regimes, and steady streaming. The fundamental contributions of this work include novel hydrodynamic regime phase diagrams demonstrating the effect of flange ratio on regime transitions, and in the investigation of their relation to qualitatively distinct patterns of vortex-vortex and vortex-structure interactions. Finally, we discuss steady streaming, identifying primary and secondary structures as a function of the governing parameters.

a) Address all correspondence to this author; maureli@unr.edu.

PLEASE CITE THIS ARTICLE AS DOI: 10.1063/5.0141889

Accepted to Phys. Fluids 10.1063/5.0141889

I. INTRODUCTION

The study of underwater vibrations of bluff bodies plays both a central and distinguished role in fundamental fluid dynamics¹⁻⁵, as well as a rich practical one in many science and engineering applications⁶⁻¹¹, spanning several orders of magnitude in time and length scales¹²⁻¹⁵. For moderately low to large Reynolds numbers, vortex shedding has been identified as one of the main mechanisms through which the energy exchange between fluid and structure takes place^{16,17}. Many, now classical, studies have investigated vortex shedding and vortexstructure interaction of oscillating bluff bodies in a quiescent fluid environment or the oscillatory flow around them^{4,5,17-19}. In two of such seminal studies, Singh⁴ and Williamson¹⁸ conducted flow visualization experiments on a fixed cylinder (among other geometries) in an oscillating flow and on an oscillating cylinder in water at rest, respectively. These works introduced the pioneering concept of hydrodynamic regime classification based on the existence and symmetry of vortex shedding. Tatsuno and Bearman⁵ conducted numerical and experimental studies on oscillations of a circular cylinder in quiescent water. They reproduced the two dimensional (2D) vortex patterns visualized by Williamson 18 and identified three dimensional sional (3D) flow patterns, in addition to Williamson's work. These regimes were found to be driven by the interplay of the governing parameters of the flow, that is, a nondimensional frequency parameter often denoted as β , or equivalently an oscillatory Reynolds number, and a nondimensional amplitude parameter, known as the Keulegan-Carpenter number²⁰ KC. In particular, Tatsuno and Bearman⁵ reported increasing instability and symmetry breaking in vortex shedding patterns as KC increases.

While many of these fundamental works focus on circular cylinders, other studies have investigated unsteady fluid-structure interaction (FSI) for different geometries and, in particular, for thin beam- or plate-like shapes^{16,21–25} which are of significant practical interest in applications such as energy harvesters^{26–29}, actuators and sensors^{30,31}, piezoelectric fans^{32,33}, atomic force microscopy^{34–37}, and biomimetic propulsion^{38–40}. While the majority of these works is concerned with the estimation of the hydrodynamic forces on the oscillating plates, Ref. 41 focused on the qualitative aspects of the flow, conducting a 2D visualization study for a broad range of governing parameters (nondimensional frequency and amplitude of oscillation) on an oscillating flat plate in a quiescent water. This work investigated the relationship between hydrodynamic force response, vortex dynamics, and other FSI mecha-

PLEASE CITE THIS ARTICLE AS DOI: 10.1063/5.0141889

Accepted to Phys. Fluids 10.1063/5.0141889

nisms. A hydrodynamic regime map was provided based on vortex shedding and symmetry breaking caused by the interplay of the oscillation governing parameters. Specifically, five different flow regimes were identified, following the philosophy of the classical studies in Refs. 4, 5, and 18. Recently, the investigation of hydrodynamic regimes has been significantly expanded in Ref. 42 where the flow physics of an oscillating thin plate with three different edges (flat, chamfered, and round edges) is investigated numerically. Remarkably, novel V-shaped and C-shaped vortex shedding regimes are identified, while also recovering the hydrodynamic regimes observed in Refs. 4, 20, and 41. In addition to elucidating the flow physics, these studies also contribute to the line of works^{22,34,43-45} concerned with the investigation the hydrodynamic loading on oscillating thin plates. It is well known that, for small KC values, the flow physics is well described by the linear Stokes flow. For this type of problem, the hydrodynamic loading can be solved with analytical and semi-analytical approaches^{21,22,34}. For large values of KC, vortex shedding and convection become dominant and lead to nonlinearities in the force response of the oscillating bluff bodies^{46,47}. Refs. 43 and 45, among others, provided numerical approaches and semi-analytical correlations to solve this nonlinear problem. These approaches were experimentally verified in Ref. 41 to be generally accurate for predicting the nonlinear hydrodynamic forces over low to moderate KC ranges. The works cited above highlight how, for moderately large KC numbers, hydrodynamic damping and power dissipation increase dramatically, and nonlinearly, with the oscillation amplitude^{23,24,42,45}. One of the primary mechanisms responsible for the increase lies in substantial vortex shedding and convection which, by transferring energy to the fluid, necessarily subtracts energy from the structure. Vortex control thus appears as a possibly viable avenue to reduce hydrodynamic damping and power dissipation in applications where these characteristics are desirable. The potential of this approach has been demonstrated via so-called shape-morphing structures where flexibility and shape of the vibrating solid can be actively controlled^{48,49}. Without recourse to active control, in an effort to mitigate the problems associated to intense vortex shedding, researchers have directed their attention to the role of different cross sections and/or aspect ratios for oscillation of sharp-edged bluff bodies^{43,50-53}. For example, in Ref. 52, underwater oscillations of a beam with thick rectangular cross section are investigated numerically to characterize the resulting hydrodynamic forces as a function of cross section aspect ratio. They reported the existence, in selected dynamic conditions, of multiple vortices shedding simultaneously from the corners of the

PLEASE CITE THIS ARTICLE AS DOI: 10.1063/5.0141889

Accepted to Phys. Fluids 10.1063/5.0141889

rectangular cross section. This phenomenon is not observed in the case of very thin cross sections⁴³. The hydrodynamic forces are seen in Ref. 52 to be sensitive to vortex-vortex and vortex-structure interactions and particularly favorable conditions may occur for the so-called "interactive vortex shedding regime", when multiple shed vortices coalesce into a single one. Departing from an ideally 2D flow, in Ref. 50, a circular disk performing oscillations along its axis is investigated experimentally with particle image velocimetry (PIV). Different aspect ratios are considered for very small amplitude and high frequency oscillation. The vortex patterns are, therein, classified in three different regimes and the vortices are observed to shed at increasing angles with respect to the disk as the aspect ratio increases. They also reported, in selected dynamic conditions, the occurence of interactive vortex shedding with the amalgamation of two vortices that are shed simultaneously from the cross section corners.

Simultaneous shedding of multiple vortices is a phenomenon also observed in Ref. 54. Therein, the underwater oscillations of an H-shaped cross section are investigated with the primary goal of understanding the effect on the hydrodynamic forces of the flange size to width ratio, that is, the ratio of the height of the added flanges on both edges of the slender plate to the width of the plate. It was there shown that it is possible to minimize hydrodynamic damping and energy dissipation via a passive vortex-structure control mechanism, driven by the selection of optimal geometry configurations, akin to interactive vortex shedding. Although in Ref. 54 it was remarked that the detailed evolution of vorticity, as modulated by geometrical and dynamical properties, plays a major role in the FSI problem, a systematic study of the flow physics and vortex-structure interaction for oscillating plates with H-shaped cross sections, or "H-plates", in the spirit of Refs. 5, 18, and 41 is currently missing. In addition, despite a possibly very rich FSI behavior exhibited by these H-plates, there has been comparatively little interest devoted to their study. Research interest is mainly focused on flow past H-plates⁵⁵⁻⁵⁹, primarily in the context of possible application to bridge vibrations in cross winds. Remarkably, in Ref. 55, the qualitative investigation of the flow past stationary H-plates and vibrating H-plates provide a fundamental insight on relevant FSI in the presence of a background lateral flow. In addition, compared to the cases of oscillating bluff bodies in a fluid at rest, the flow physics is slightly modified by the presence of the so-called Froude-Krylov force⁴⁷. Thus, we conclude that qualitative and quantitative understanding of the physics of underwater oscillations of H-plates remain

PLEASE CITE THIS ARTICLE AS DOI: 10.1063/5.0141889

Accepted to Phys. Fluids 10.1063/5.0141889

relatively limited.

Besides the primary flow which results in vortex shedding, oscillatory systems possess a secondary flow known as steady streaming^{60,61}. This flow takes place in the background of the main unsteady fluid motion as a result of the transverse periodic oscillatory motion of a body submerged in a fluid. Several studies have investigated the phenomenon via analytical^{2,62-66}, numerical^{42,67-70} and experimental approaches⁷¹⁻⁷³ to highlight the interaction of steady streaming and the bluff body and estimate this background flow. In particular, Stuart⁷⁴ developed a classification criteria for the steady streaming of oscillating cylinders. Therein, steady streaming is classified based on the so called steady streaming Reynolds number Re_s . The critical value for $Re_s \approx 1$ is where the steady streaming is governed by the full Navier-Stokes equations. For $Re_s \leq 1$, the flow field is governed by the Stokes equation and the boundary layer generated by the oscillation is denoted as "Stokes boundary layer". For Re_s ≥ 1, a secondary boundary layer is present for oscillating cylinders. In Ref. 68, particle trapping in the streaming cells of an oscillating cylinder is investigated in a numerical and analytical study. The speed of the trapped particles is found to be increasing as the Reynolds number increases. The particles outside the streaming cell, which is located in the secondary boundary layer, are repelled as they are unaffected by the oscillation of the cylinder, thereby confirming the secondary boundary layer as the dominant driver of steady streaming. Beyond circular cylinders, Ref. 69 investigated 3D streaming patterns of an oscillating flat plate via a numerical analysis over a broad range of governing parameters. These classical and recent studies provide key understanding on distinguishing the structure of steady streaming for thin plates from that of cylinders. However, no such investigation exists for the case of H-shaped cross sections.

To address the above knowledge gaps, in this paper, we investigate the role of flanges in an H-plate configuration on the flow physics of underwater vibrations, via an experimental approach. For a broad range of governing parameters, including frequency, amplitude, and flange size, we perform PIV experiments and present qualitative and quantitative results of the flow patterns, vorticity, and steady streaming. We identify the hydrodynamic regimes as a function of aforementioned parameters. Specifically, we present a phase diagram for the occurrence of the hydrodynamic regimes for each flange ratio. By carefully examining the occurrence of these regimes for each flange, we discover that transitions between hydrodynamic regimes are progressively delayed as the flange ratio increases. For the identified

PLEASE CITE THIS ARTICLE AS DOI: 10.1063/5.0141889

Accepted to Phys. Fluids 10.1063/5.0141889

hydrodynamic regimes, we present a qualitative description based on flow visualization over a period of oscillation. More in detail, we introduce novel quantitative and qualitative results on the time history of vortex-structure and vortex-vortex interactions and their dependence on the H-plate geometry and dynamical conditions. Among the qualitative differences of vortex formation with different flange ratios, we observe that multiple simultaneously shed vortices dissipate at different instants and the dissipation time scales increase as flange ratio increases. We use previously presented formulations^{41,75} to predict the hydrodynamic forces on the H-plates from PIV data, recovering qualitative agreement with the numerical results of Ref. 54. Finally, in a first investigation of its kind, we study the inner flow component of the steady streaming of H-plates and present the effect of flanges on the steady streaming with both qualitative and quantitative results. We observe similar structures to the streaming characteristics of other bluff bodies in literature and report on the dependence of velocity flux, in the neighborhood of the H-plate, on the flange ratio.

The rest of this paper is organized as follows. In Section II, we introduce experimental methods which include our PIV approach, the estimation of steady streaming characteristics, and the methods of flow visualization. In Section III, we present and discuss the experimental results including determination of flow regimes, qualitative path line evaluation, vortex-structure interaction, estimation of hydrodynamic force, and steady streaming. Finally, conclusions are presented in Section IV.

II. MATERIALS AND EXPERIMENTAL METHODS

In the present study, we investigate the effect of flanges on the flow physics induced by harmonic oscillations of submerged plates, by focusing on a 2D flow field whose domain encompasses a cross section of the structure. With reference to the schematics in Fig. 1, the motion of the H-plate is a prescribed rigid translation along the y-axis, described by $\delta(t) = A\sin(\omega t)$, where A is the amplitude, ω is the angular frequency, and t is the time variable.

PLEASE CITE THIS ARTICLE AS DOI: 10.1063/5.0141889

Accepted to Phys. Fluids 10.1063/5.0141889

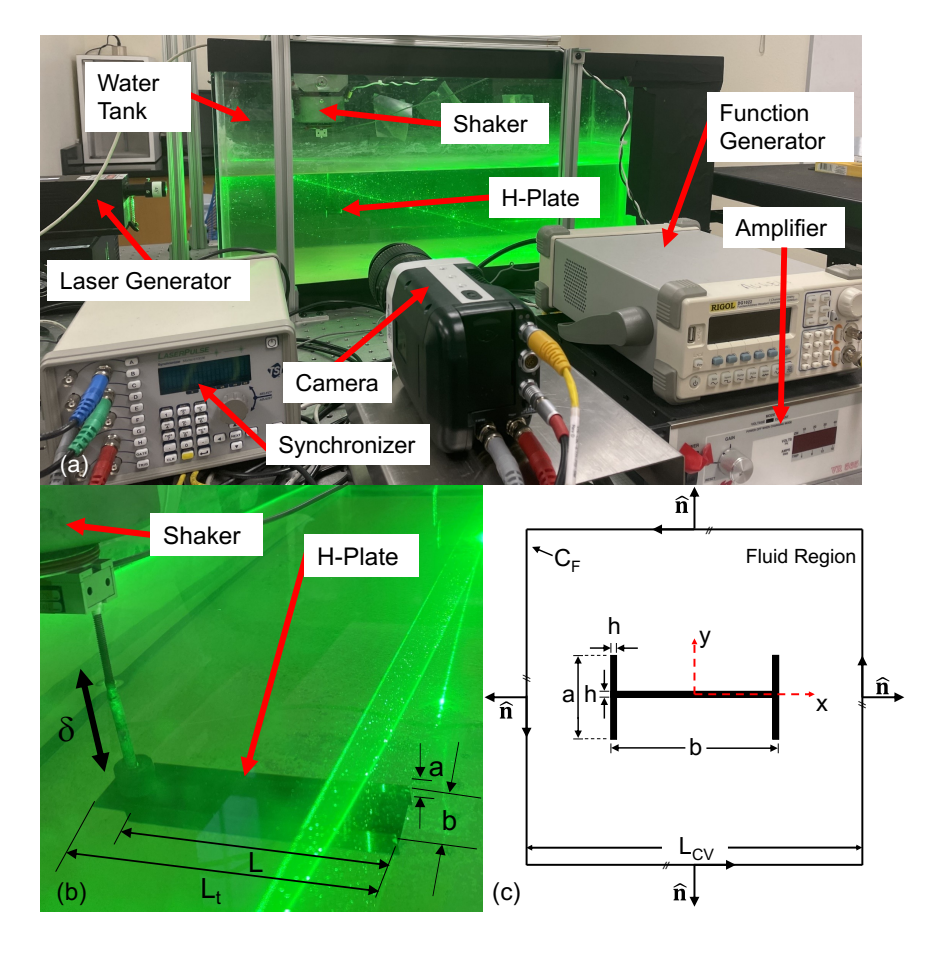


FIG. 1. (a) View of the experimental setup. (b) Close up view of the plates and relevant nomenclature. (c) Contour and control volume for force and streaming flux estimation.

A. Experimental Setup

All experiments are performed in a large 150-liter $910 \times 460 \times 430 \,\mathrm{mm^3}$ water tank, see Fig. 1(a). We use seven different stainless steel plates which share the same total length $L=120\,\mathrm{mm}$, effective length $L=112\,\mathrm{mm}$, width $b=27.75\,\mathrm{mm}$, and thickness $h=0.7\,\mathrm{mm}$, see Fig. 1(b). The plates are constructed with different flange sizes a to produce flange ratios $\chi=a/b$ in the range 0–0.6, with an increment of 0.1. This choice allows us to

PLEASE CITE THIS ARTICLE AS DOI: 10.1063/5.0141889

Accepted to Phys. Fluids 10.1063/5.0141889

explore the parameter range previously discussed in Ref. 54. Here, the "effective length" indicates the part of the plate not covered by its attachments to the mechanical excitation system. Note that the plate with $\chi=0$ does not have flanges and is designed to replicate the experimental conditions in Ref. 41; therefore, we will often omit the discussion of the results for this configuration. Note that the plates are hand-fabricated and very minor deviations from perpendicularity may occur. However, care was taken to minimize these deviations. Similarly, test articles are repeatedly removed and reinstalled in the fixtures for the experiments and minor misalignments may occur that may cause slight deviations from the ideal purely transverse translation of the plate in the fluid. As we limit the investigation to regimes in which we do not pursue effects such symmetry breaking or onset of chaos, we posit that these possible defects and misalignment are not affecting the flow in an appreciable way. Also, the large number of experiments is expected to smooth out the effect of randomness in the experimental conditions.

Water is selected as the working fluid. All experiments are conducted at room temperature with the assumption of standard values of density and dynamic viscosity of water as $\rho = 998.2 \,\mathrm{kg} \,\mathrm{m}^{-3}$ and $\mu = 1.003 \times 10^{-3} \,\mathrm{Pa} \,\mathrm{s}$, respectively. Thus, the fluid kinematic viscosity is estimated as $\nu = \mu/\rho = 10^{-6} \,\mathrm{m^2 \, s^{-1}}$. Note that the laboratory in which the experiments are performed is kept at reasonably constant temperature as to minimize possible drifts in viscosity and density due to temperature changes. Thus, we expect a less than 4% change in the viscosity values. The H-plates are submerged deep enough under the water free surface to minimize the effect of surface waves and the presence of the solid wall at the bottom of the tank. To provide the desired motion to the plate, a Vibration Research VR520 shaker is mounted to the plate with a connecting rod, see Fig. 1(b). Frequency $f = \omega/(2\pi)$ and amplitude A are specified with a function generator. The generated signal is then amplified with a power amplifier and finally transmitted to the shaker. By controlling the H-plate geometry and the excitation characteristics, we can prescribe the governing nondimensional parameters of this experimental campaign, which are the nondimensional frequency parameter β , the nondimensional amplitude parameter ϵ , and the nondimensional flange ratio χ , see Ref. 54. These are defined via $\beta = fb^2/\nu$, see also Ref. 76, $\epsilon = A/b$, and $\chi = a/b$, respectively.

A total of 2400 tests were performed spanning the range of $\beta \in [90, 2000]$, $\epsilon \in [0.01, 0.2]$, and $\chi \in [0,0.6]$, corresponding to a range of frequencies between 0.065 and 2.6 Hz,

PLEASE CITE THIS ARTICLE AS DOI: 10.1063/5.0141889

Accepted to Phys. Fluids 10.1063/5.0141889

amplitudes between 0.278 and 5.55 mm, and flange sizes of 0 to 16.65 mm. For ease of comparison with existing literature, it is convenient to express these parameter ranges also in terms of the system's Reynolds number Re = $2\pi\beta\epsilon$, and Keulegan–Carpenter number KC = $2\pi A/b$, so that Re \in [6, 2500] and KC \in [0.063, 1.3], respectively.

To minimize undesired dynamics in the system, we constrain our excitation frequency to be well below the estimated natural frequency of the submerged structure. This is calculated for a flat plate to be approximately 5.7 Hz using Chu's formula as in Ref. 77. The flanges increase significantly the moment of inertia of the cross section and, therefore, both its in vacuo and submerged natural frequencies. Thus, these values are considerably higher than the maximum excitation frequency of 2.6 Hz adopted in this work.

B. Particle Image Velocimetry Experiments

We use a time-resolved planar PIV system from TSI, Inc. to investigate 2D velocity fields during the oscillation of the H-plates. A green laser sheet produced by a 5 W continuous wave 532 nm laser beam generator (OptoEngine, LLC) is placed next to the water tank to illuminate a vertical plane containing a cross section of the oscillating H-plate. Silver coated hollow spherical glass particles with a diameter of $10\,\mu\mathrm{m}$ are used as seed. To avoid undesired 3D effects, as discussed in Ref. 41, the laser sheet is kept at an optimum distance from both clamped and free end of the H-plate. Image artifacts may appear in the digital images due to less than ideal exposure, due to reflections and other optical effects. To minimize these artifacts, three sides of the water tank are covered by opaque material thus leaving only one side for the laser optical access. Similarly, the stainless steel material of the test articles is painted in matter black with non reflective spray paint.

The illuminated plane is imaged with a Phantom Miro 120 high-speed camera. Shutter opening and timing on the high speed camera are carefully adjusted to prevent overexposure. We select a resolution of 1920×1200 pixels with 12 bits per pixel for all cases. During the experiments, we position the camera such that the field of view is at least $1.5b \times 1.5b$. The H-plate is kept in the center of the field of view. We capture flow images after at least 20 cycles of oscillation have elapsed so that possible transients in the time history of the data are eliminated. To avoid interactions between two consecutive experiments, we make sure that sufficient amount of time has passed before starting the next experiment. While

PLEASE CITE THIS ARTICLE AS DOI: 10.1063/5.0141889

Accepted to Phys. Fluids 10.1063/5.0141889

capturing a harmonic motion, aliasing can lead to misleading results. Therefore, for each β value, we select the acquisition frequency such that the time history of the data is adequately resolved to eliminate such possibilities.

To minimize experimental uncertainties due to calibration drift, we perform an optical calibration by determining the width of the plate during the post processing of the digital images, in terms of pixels and identifying the corresponding length scale. The calibration is performed for all quantitative results reported in this work. For post-processing of the images, we use TSI INSIGHT 4G software. The post-processing algorithm adopts a recursive Nyquist Grid with central difference offset method to extract the velocity fields by using a multi-grid method with 50 % overlap of the interrogation area. Furthermore, we select an interrogation area decreasing from 64×64 to 32×32 , while ensuring that there are at least 10 particles in the interrogation area. We use a FFT correlator technique for the correlation engine and a Gaussian peak with signal-to-noise ratio of 1.5 for the peak engine. To validate the velocity vector data during processing and post processing of the velocity field, we use a local validation method which checks the velocity data using a median test method within the neighborhood a grid size of 5×5 with a tolerance of 2 pixels. The output of the post-processing stage consists of 2D velocity fields, resolved at least 100 equally spaced sample time points per oscillation period.

C. Pathline tracing and visual interpretation

The investigation of the flow physics of the H-plates is conducted, leveraging the acquired PIV data, on a total 2400 experiments in which we systematically vary the flow governing parameters in the ranges $\beta \in [90, 2000]$, $\epsilon \in [0.01, 0.2]$, and $\chi \in [0, 0.6]$. Similarly to our previous approach in Ref. 41, we use ImageJ software to process the images and produce pathlines to assess the qualitative characteristics of the flow. Specifically, PIV images are first digitally stacked and, successively, a maximum intensity projection is used on a subset of the images. Image clarity is also enhanced by adjusting the brightness and contrast values as needed. By doing so, we simulate digitally the effect of having the camera shutter open so that the motion of the seeding particles around the H-plate is tracked into streaks as in a long exposure mode. In the end, a set of pathlines is produced at different time intervals during the oscillation.

PLEASE CITE THIS ARTICLE AS DOI: 10.1063/5.0141889

This is the author's peer reviewed, accepted manuscript. However, the online version of record will be different from this version once it has been copyedited and typeset

Accepted to Phys. Fluids 10.1063/5.0141889

By visually interpreting the motion of particles and the structure of the pathlines, we distinguish different flow dynamic regimes for different combinations of the governing parameters. Specifically, to classify these regimes, following in part the approach in Ref. 41, we consider the following set of criteria: (i) particle trajectory, (ii) number of vortices existing in the flow field, (iii) interaction patterns between vortices, (iv) change of vortex shape and size from the two tips of the H-plates, and (v) elapsed time before vortex dissipation around the H-plates.

D. Estimation of Steady Streaming

To assess the effect of the flanges on streaming characteristics, we study the instantaneous fluxes over a fixed control domain surrounding the oscillating H-plate. The domain is a square of side L_{CV} , see Fig. 1(c). Time-resolved fluxes $q_s(t)$ are estimated as:

$$q_s(t) = \frac{1}{A\omega L_{CV}} \int_{-L_{CV}/2}^{+L_{CV}/2} \boldsymbol{u}(\boldsymbol{x}, t) \cdot \hat{\boldsymbol{n}} \, \mathrm{d}\ell$$
 (1)

III. RESULTS AND DISCUSSIONS

A. Phase diagrams of the hydrodynamic regimes

Following the approach in Ref. 41, digital images of the flow field are used to construct pathlines of the flow by mimicking the photographic technique of long exposure with digital methods. Qualitative analysis of such pathlines, combined by the classification criteria given in Section II C, leads to the identification a number of different characteristic dynamic

PLEASE CITE THIS ARTICLE AS DOI: 10.1063/5.0141889

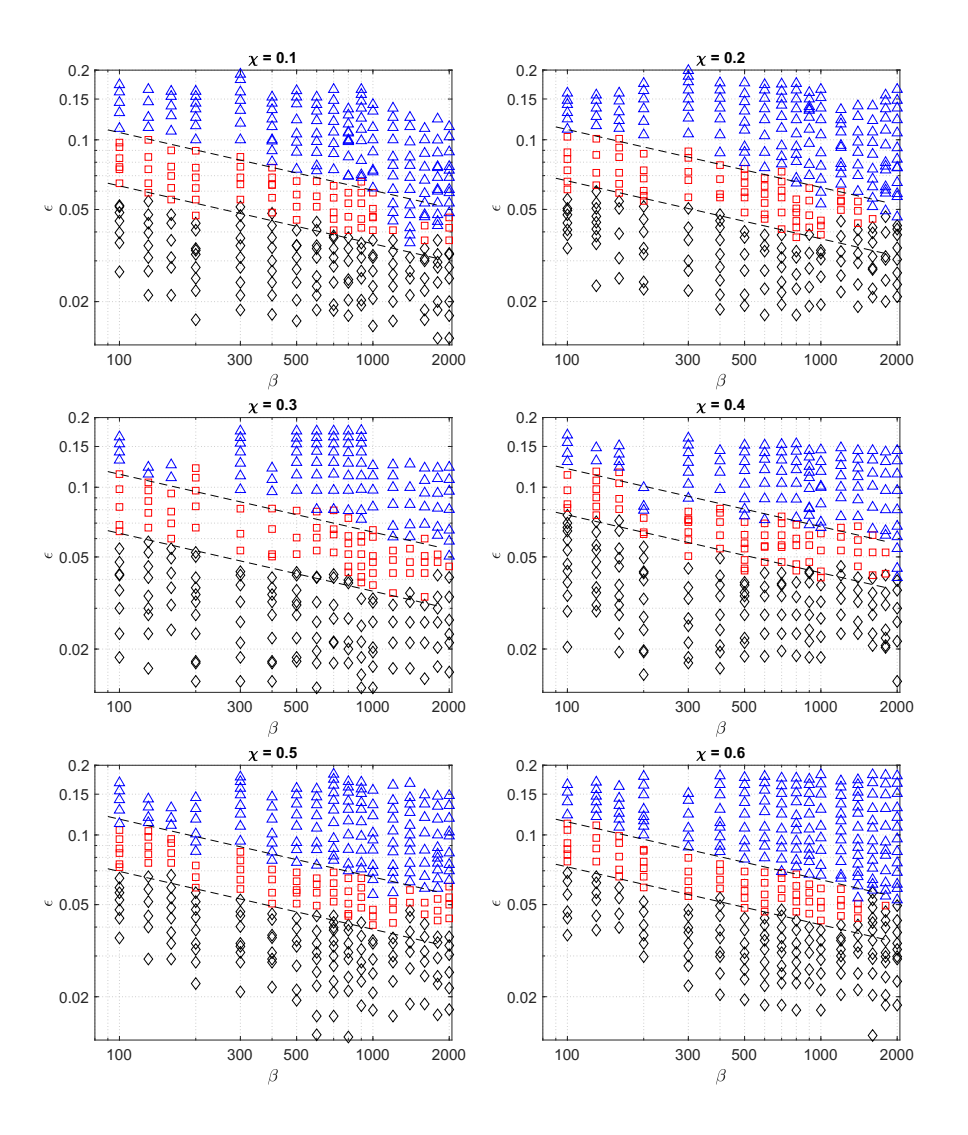


FIG. 2. Phase diagrams of hydrodynamic regimes of the six H-plates from $\chi=0.1$ to $\chi=0.6$. Dashed lines represent identified approximate transitions between the hydrodynamic regimes. Markers indicate regimes experimentally observed. Regime A: \Diamond , Regime B: \Box , Regime C: \triangle .

PLEASE CITE THIS ARTICLE AS DOI: 10.1063/5.0141889

Accepted to Phys. Fluids 10.1063/5.0141889

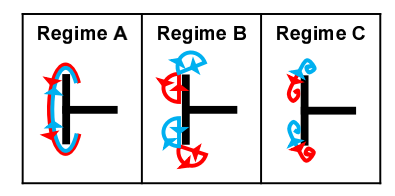


FIG. 3. Sketches of the salient features used to differentiate among the hydrodynamic regimes. Red and blue traces exemplify representative particle trajectories during the upstroke and downstroke, respectively.

regimes for the flow. The occurrence of these regimes is dependent on the interplay of the governing parameters β , ϵ , and χ . Similarly to the study of flat plates⁴¹, experimental results on the hydrodynamic regimes can be presented in the form of phase diagrams as a function of the governing parameters.

Figure 2 displays such phase diagrams for each of the six non-zero flange ratios explored for our H-plate configurations in log-log scale. Each panel is constructed to show the extent of different hydrodynamic regimes as a function of β and ϵ , as the flange ratio χ increases in panels (a) through (f). Based on experimental observations, each panel in Fig. 2 displays three main regions in the (β, ϵ) -plane, approximately separated by dashed lines in each panel, determined by the occurrence of qualitatively different hydrodynamic regimes. These regions correspond to three main distinct hydrodynamic regimes are denoted with letters A through C. While the nomenclature follows that of Ref. 41, the details of observed flow structures differ due to the presence of the flanges. For ease of presentation, sketches of the salient features used to differentiate among the regimes appear in Fig. 3.

More in detail, with "regime A" we indicate a flow regime in which particles exhibit limited periodic motion in the vicinity of the flanges of the H-plates. Within this regime, the amplitude of such motion appears generally independent of the flange ratios. All experiments show particles adjacent to the solid structure displacing over a small distance along the flange. Interestingly, particles near the flange tips are observed to perform curved trajectories around the tips during an oscillation cycle.

We indicate with "regime B" a flow regime in which the amplitude of particle motion increases and the particle trajectory becomes more complex. Specifically, during half a cycle of oscillation, particles adjacent to the flanges are observed to move against the flange side

PLEASE CITE THIS ARTICLE AS DOI: 10.1063/5.0141889

Accepted to Phys. Fluids 10.1063/5.0141889

and recirculate in the suction region behind and under the flange in the first quarter cycle. In the second quarter cycle, particles from the suction region are ejected away from the plate along an almost-horizontal direction and travel a distance comparable to the flange size before reversing their motion and approximately closing their trajectory in a "figure-8" pattern. A similar, but not identical, figure-8 pattern was observed for the flat plate in Ref. 41. In the second half cycle, as the motion of the H-plate is reversed, the particle trajectories are largely symmetric to those of the first half cycle and mirrored with respect to the H-plate width. For this reason, the primary flow structures that discriminate regime B are the "double figure-8" patterns.

Finally, we denote with "regime C" a regime in which particle trajectories indicate full vortex shedding from each tip of the flanges, in a total of two pairs for each half cycle of oscillation. This is in contrast with what was observed in the case of the flat plate, for which only a pair of vortices is shed during each half cycle. Generally speaking, the shed vortices are short lived and observed to dissipate within a fraction of half a period.

Interestingly, compared to the vortex dynamics of flat plates, we are not able to observe strong indications of regime D^{41} , in which the vortex formed in a previous half cycle survives and interacts with the vortex formed in the cycle of interest. However, in some rare cases at the upper boundaries of our ϵ range, we observe characteristics of this regime, where separated layer on the leading edge briefly interacts with the vortex of the previous case for a short fraction of a period of oscillation. Due to the difficulty in unambiguously determining these occurrences, we focus in the remainder of the paper on the discussion of the above mentioned three regimes which can instead be clearly distinguished. Remarkably, the disappearance of regime D-like structures should be ascribed to the presence of even the smallest flanges considered in this work, highlighting the important qualitative differences of these structural modifications on the development of the resulting flow. In other words, complex flow dynamics observed in other works for different geometries, including symmetry breaking $^{41,78-81}$ and transition to chaos and substantially 3D flow⁵, are delayed as the flange ratio increases.

For each flange ratio, the dashed lines in each panel of Fig. 2 indicate approximate regime transitions in the log-log plane of the governing parameters β and ϵ . Both transitions from regime A to regime B and from regime B to regime C are triggered by the interplay of β and ϵ and are observed to occur approximately along a line with slope -1/4 in log-log

PLEASE CITE THIS ARTICLE AS DOI: 10.1063/5.0141889

Accepted to Phys. Fluids 10.1063/5.0141889

scale. Therefore, since these lines can be described via $\log \epsilon = \log \alpha - (1/4) \log \beta$, with $\log \alpha$ the intercept of the line, this observation suggests that there exists a critical ϵ at which transitions occur, given by $\epsilon_{\rm cr} = \alpha \beta^{-1/4}$. In terms of a critical Reynolds number⁴¹, the scaling can similarly be identified as ${\rm Re_{cr}} \sim \beta^{3/4}$. Interestingly, the dependence of the critical $\epsilon_{\rm cr}$ on $\beta^{-1/4}$ was observed in our previous works for different plate geometries^{41,43}. More intriguing is the observation that the same scaling power was identified in various studies on oscillating circular cylinders in quiescent flows and on fixed cylinders in oscillating flows, albeit in terms of the Keulegan-Carpenter number, given by ${\rm KC} = 2\pi A/D$ for a cylinder of diameter D, see Refs. 82 and 83. The origin of the scaling was ascribed to instabilities of the oscillating boundary layers around the cylinder⁸⁴. The fact that the same scaling appearing over many different geometries and dynamic conditions seem to suggest the possibility that this is a "universal phenomenon" in oscillating boundary layer dynamics.

To further investigate the effect of the flange ratio on the delaying of the hydrodynamic transitions between regimes, we identify the numerical values of the intercepts $\log \alpha$ on our phase planes, and collect the values of α for the A–B and B–C transitions as a function of χ in the diagram in Fig. 4. The α values for the case $\chi=0$ are obtained from the phase diagram in Ref. 41 and confirmed by independent experiments conducted on a flat plate. It can be observed that for both transition types, transition is delayed to larger values of $\epsilon_{\rm cr}$ as the flange ratio increases. Specifically, for the case of flat plate, the A-B transition occurs at approximately $\alpha = 0.15$ and the B-C transition occurs at approximately $\alpha = 0.25$. For the H-plates, the A-B transitions occur approximately in the range $\alpha \in [0.2, 0.23]$ while the B-C transitions occur approximately in the range $\alpha \in [0.34, 0.37]$. However, the sensitivity of α on χ decreases as χ increases. This "saturation" could be explained by considering the diminishing mutual influence of the separated flow regions at the flange tips as the flange size increases and, therefore, as the physical separation of the separated flow regions increases. This peculiar vortex shedding was previously identified as "interactive vortex shedding" 50,54 and correlated with substantial changes in the hydrodynamic forces on the structure. In Section III C, we will further discuss the significant differences observed on vortex formation and dynamics on different H-plates.

PLEASE CITE THIS ARTICLE AS DOI: 10.1063/5.0141889

Accepted to Phys. Fluids 10.1063/5.0141889

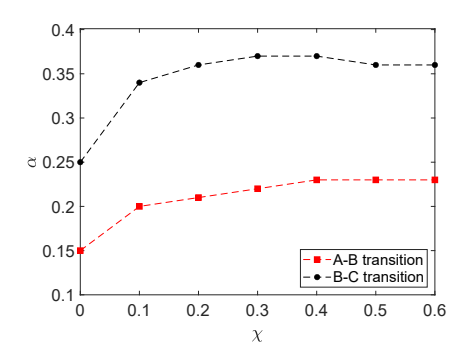


FIG. 4. Intercepts of the transition lines for each flange ratio. The coefficient α establishes a correlation between the critical $\epsilon_{\rm cr}$ and β as $\epsilon_{\rm cr} = \alpha \beta^{-1/4}$ for both A–B and B–C transition types. These transitions are likely dependent on instabilities of the oscillating boundary layers.

B. Flow physics of the hydrodynamic regimes

In Figs. 5, 7, and 9, we present, superimposed on actual experimental pictures, pathlines determined with the digital imaging method described above. In addition to the these figures, in Figs. 6, 8, and 10, we present instantaneous nondimensional velocity vector fields merged with instantaneous streamlines obtained from postprocessing of the PIV velocity data. For ease of presentation, velocity values are normalized with the characteristic velocity of the plate ωA . In each figure, a specific combination of β and ϵ is selected to demonstrate a particular hydrodynamic regime, as described in Figs. 2 and 3. Two distinct flange ratios are displayed to illustrate the effect of varying χ on the details of the flow field within each hydrodynamic regime. For the two flange ratios displayed in the description of a single hydrodynamic regime, the H-plate is moving through the flow with identical prescribed displacement and, therefore, velocity. These figures display the time evolution of the flow over one period T by capturing instantaneous snapshots from t = T/4 to t = T, with an increment of T/4. Similarly, the velocity vector fields and the streamlines represent the instantaneous flow field at the time shown. Small disturbances, that can be noted in the pathlines, the velocity vector fields, and the streamlines located on the right side of the H-plates, are caused by uneven illumination, as the light source is on the left of the flow field, resulting in less illumination of the right side.

Figure 5 illustrates time snapshots of the flow pathlines observed in regime A at $\beta=700$ and $\epsilon=0.034$, for $\chi=0.1$ and 0.5, respectively. For the same experimental conditions, Fig. 6 displays instantaneous velocity vector fields and superimposed streamlines. In regime A, the pathlines exhibit temporal symmetry as well as reflection symmetries about the x-and y-axis, as also confirmed by the shown streamlines at t=2T/4 and t=T, where the H-plate has peak speed. Common characteristics of the flow field in this regime are, besides the above mentioned symmetry, the limited periodic motion of the particles in the vicinity of the H-plate, and the absence of vortical structures. For all χ values, pathlines tend to form C-shape patterns while they wrap around the flanges during the oscillation, similar to what observed in the case of flat plates⁴¹.

However, as χ increases, the particles trajectories deform from a circular shape for $\chi=0.1$ to a more elongated one for $\chi=0.5$ as the pathlines follow the flange lengths. Remarkably, the spacing between adjacent streamlines in the suction side of the H-plate reduces significantly for the larger χ values at t=2T/4 and t=T, indicating substantial increase in the velocity field even if the motion of the H-plate is invariant among the different χ values. In addition, as the flange ratio increases, we note increased curvature of the streamlines in the same region, suggesting the presence of concentrated low-pressure areas in the vicinity of the trailing edge.

Further away from the plate, the motion of the particles is negligible, which confirms the dominant role of viscous effects in this regime. The streamlines also suggest separation of the flow from the sharp edges of the plate⁴⁷.

Regime B. The characteristics of regime B, indicated with red squares in Fig. 2, are generally observed for all flange ratios across the entire β range for intermediate values of ϵ . More in detail, regime B is observed, for $\chi=0.1$, at around $0.065<\epsilon<0.097$ for $\beta=100$ and $0.037<\epsilon<0.046$ for $\beta=2000$. For $\chi=0.6$, this regime is observed at around $0.077<\epsilon<0.011$ for $\beta=100$ and $0.044<\epsilon<0.051$ for $\beta=2000$.

PLEASE CITE THIS ARTICLE AS DOI: 10.1063/5.0141889

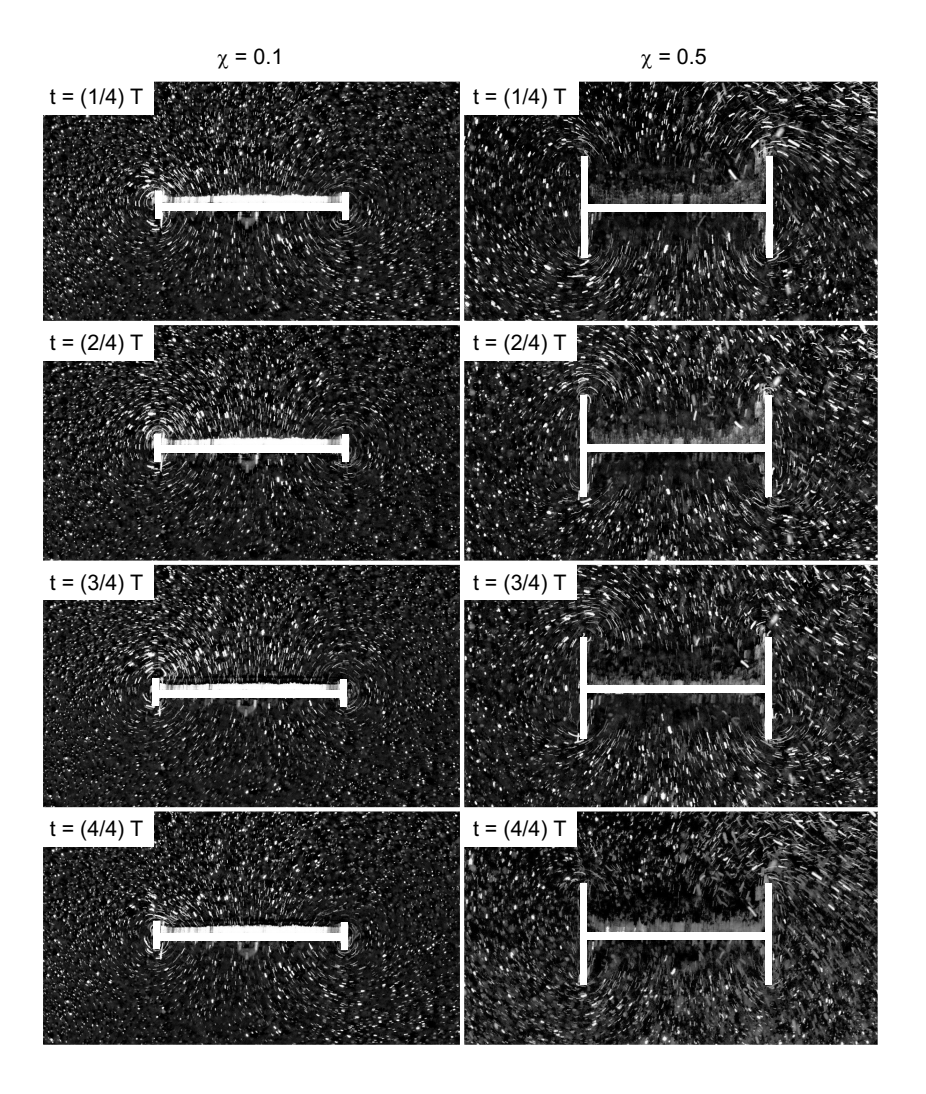


FIG. 5. Particle pathlines at four instants of time in one oscillation cycle of regime A for $\beta = 700, \epsilon = 0.034$, and $\chi = 0.1$ (left column) and 0.5 (right column).

PLEASE CITE THIS ARTICLE AS DOI: 10.1063/5.0141889

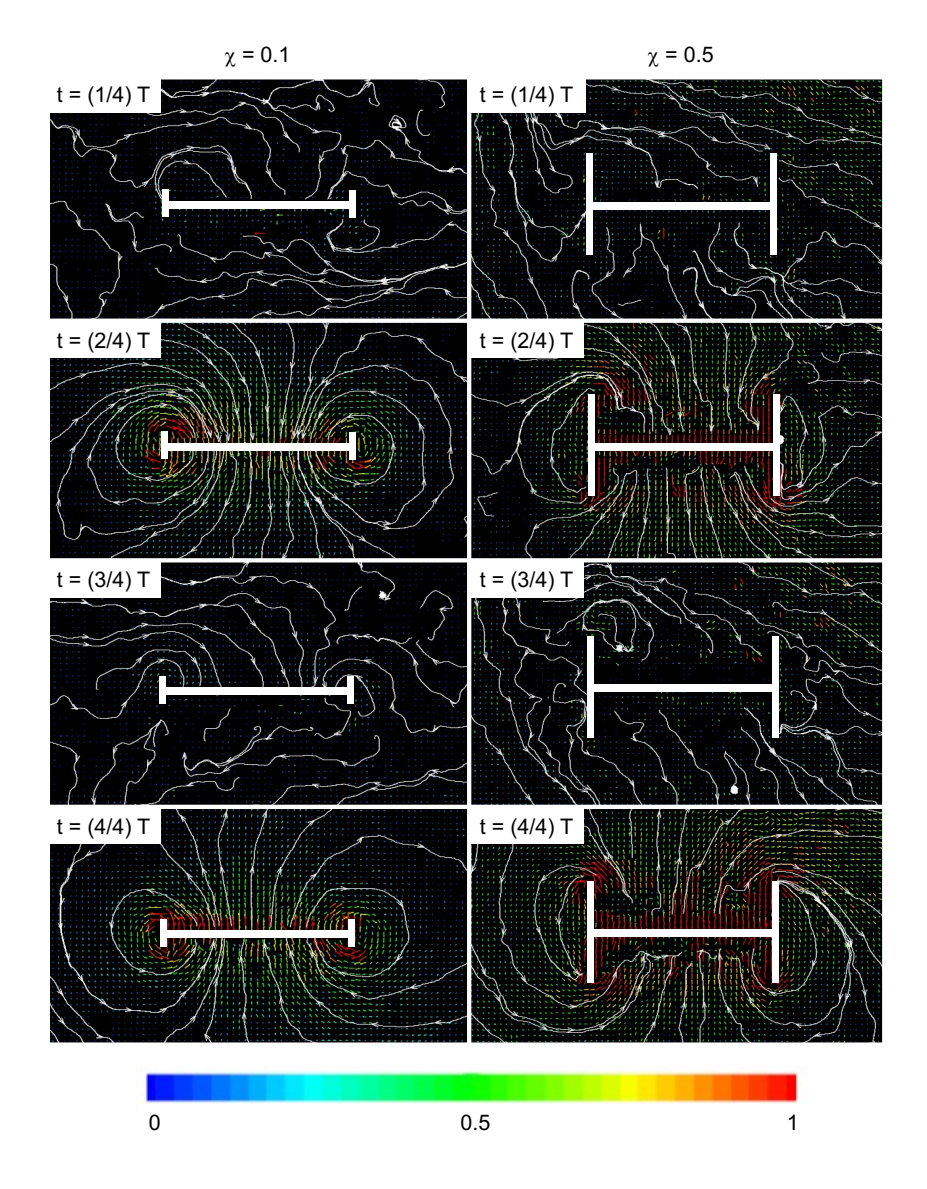


FIG. 6. Instantaneous nondimensional velocity vector fields and superimposed streamlines at four instants of time in one oscillation cycle of regime A for $\beta=700, \epsilon=0.034$, and $\chi=0.1$ (left column) and 0.5 (right column).

PLEASE CITE THIS ARTICLE AS DOI: 10.1063/5.0141889

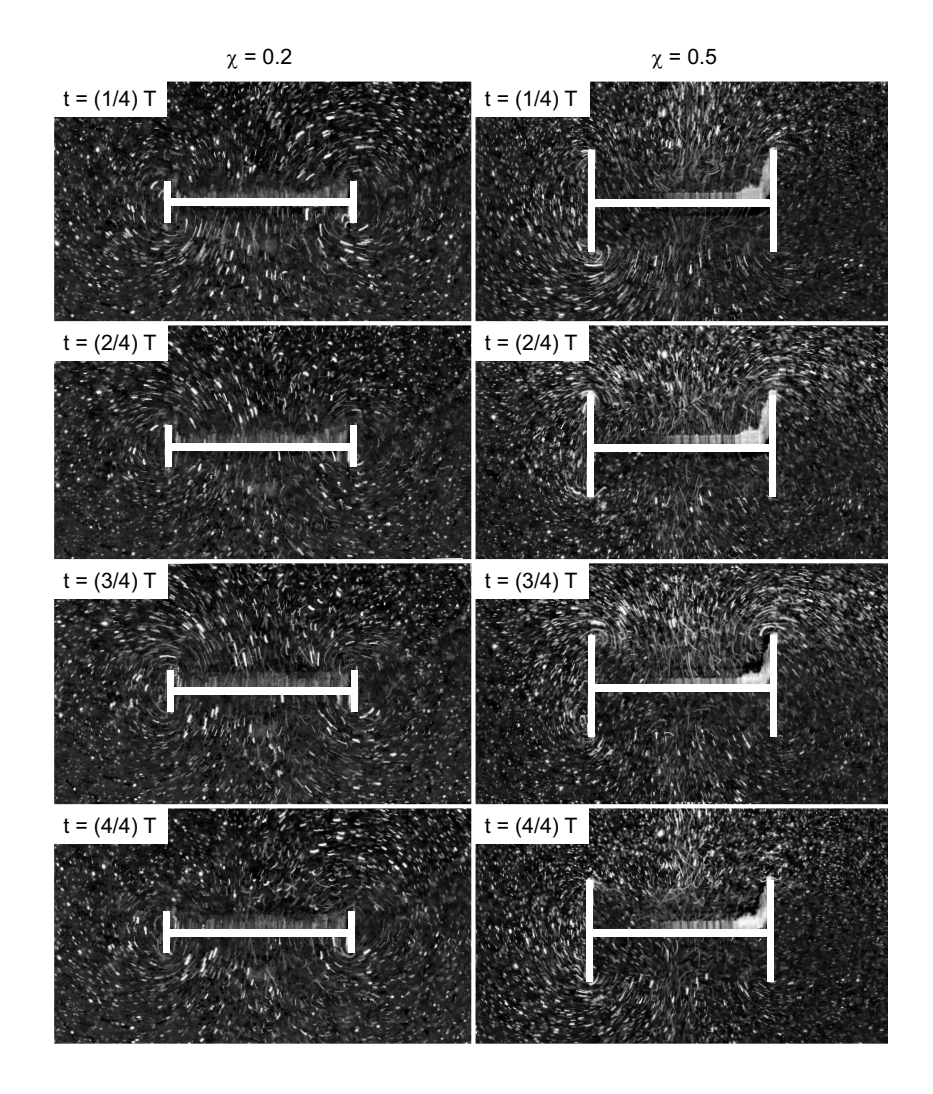


FIG. 7. Particle pathlines with superimposed streamlines at four instants of time in one oscillation cycle of regime B for $\beta = 500, \epsilon = 0.06$, and $\chi = 0.2$ (left column) and 0.5 (right column).

PLEASE CITE THIS ARTICLE AS DOI: 10.1063/5.0141889

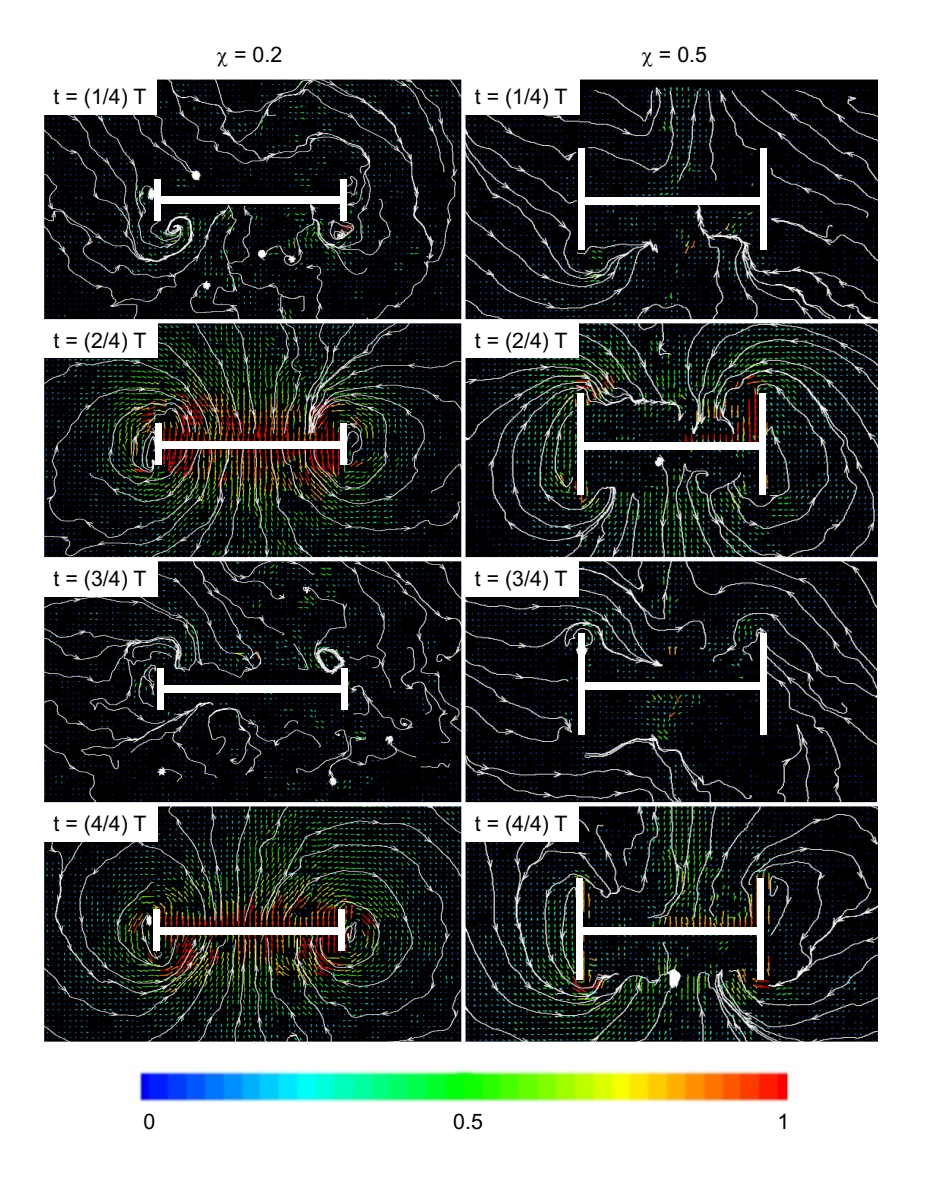


FIG. 8. Instantaneous nondimensional velocity vector fields and superimposed streamlines at four instants of time in one oscillation cycle of regime B for $\beta=500, \epsilon=0.06$, and $\chi=0.2$ (left column) and 0.5 (right column).

PLEASE CITE THIS ARTICLE AS DOI: 10.1063/5.0141889

Accepted to Phys. Fluids 10.1063/5.0141889

Figure 7 shows the pathlines of regime B observed at $\beta=500, \epsilon=0.06$ for $\chi=0.2$ and 0.5, respectively. For the same experimental conditions, Fig. 8 displays instantaneous velocity vector fields and superimposed streamlines. Particles in this regime possess substantial motion in the vicinity of the plate. Similar, but not identical, to the figure-8 pattern in Ref. 41, particles tend to move further away from the edges of the H-plates and their trajectories resemble the double figure-8 patterns sketched in Fig. 3. These should be not considered fully developed vortical structures but precursors to vortex shedding.

The main effect of the H-plate cross section is evident at the leading edge of the motion. As displayed by streamlines at t=2T/4 and t=T, the separation of the flow at the leading edge causes prominent curvature in the pathlines than what observed in regime A. This results in a secondary circulation, in addition to the circulation at the trailing edge, during both upstroke and downstroke of the H-plates, see Fig. 3. At the end of one oscillation period, a closed loop "figure-8" path is thus observed at all four tips of the H-plate. As χ increases, the "figure-8" paths are elongated, as confirmed by both pathlines and streamlines, and their characteristic size progressively increases beyond the flange size.

As the flange ratio increases, the two figure-8 pathlines of the particles corresponding to the upstroke and downstroke tend to move apart from each other. As a result, their overlapping region, adjacent to flange observed for small χ values, progressively disappears and the two half-trajectories become spatially separate. Similar to regime A, the spacing between adjacent streamlines in the suction side of the H-plate reduces substantially for the larger χ values at t=2T/4 and t=T, which pinpoints a drastic increase in flow velocity, which is observed in the velocity vector fields as well. In addition, curvature of the streamlines is observed to increase in the same region with increasing flange ratio, suggesting the presence of concentrated low-pressure areas in the vicinity of the trailing edge.

Regime C. Regime C occurs across the entire β range covered, for relatively higher ϵ values, decreasing as β increases, for all flange ratios and is indicated with blue triangles in Fig. 2. This regime is observed for $\chi=0.1$ between approximately $0.11<\epsilon<0.17$ for $\beta=100$ and $0.048<\epsilon<0.11$ for $\beta=2000$. For $\chi=0.6$, this regime is seen between approximately $0.12<\epsilon<0.17$ for $\beta=100$ and $0.052<\epsilon<0.18$ for $\beta=2000$.

In Fig. 9, we present time snapshots of the flow pathlines representative of this regime at $\beta = 500$, $\epsilon = 0.1$ for $\chi = 0.2$ and 0.6, respectively. For the same experimental conditions, Fig. 10 displays instantaneous velocity vector fields and superimposed streamlines. Note

PLEASE CITE THIS ARTICLE AS DOI: 10.1063/5.0141889

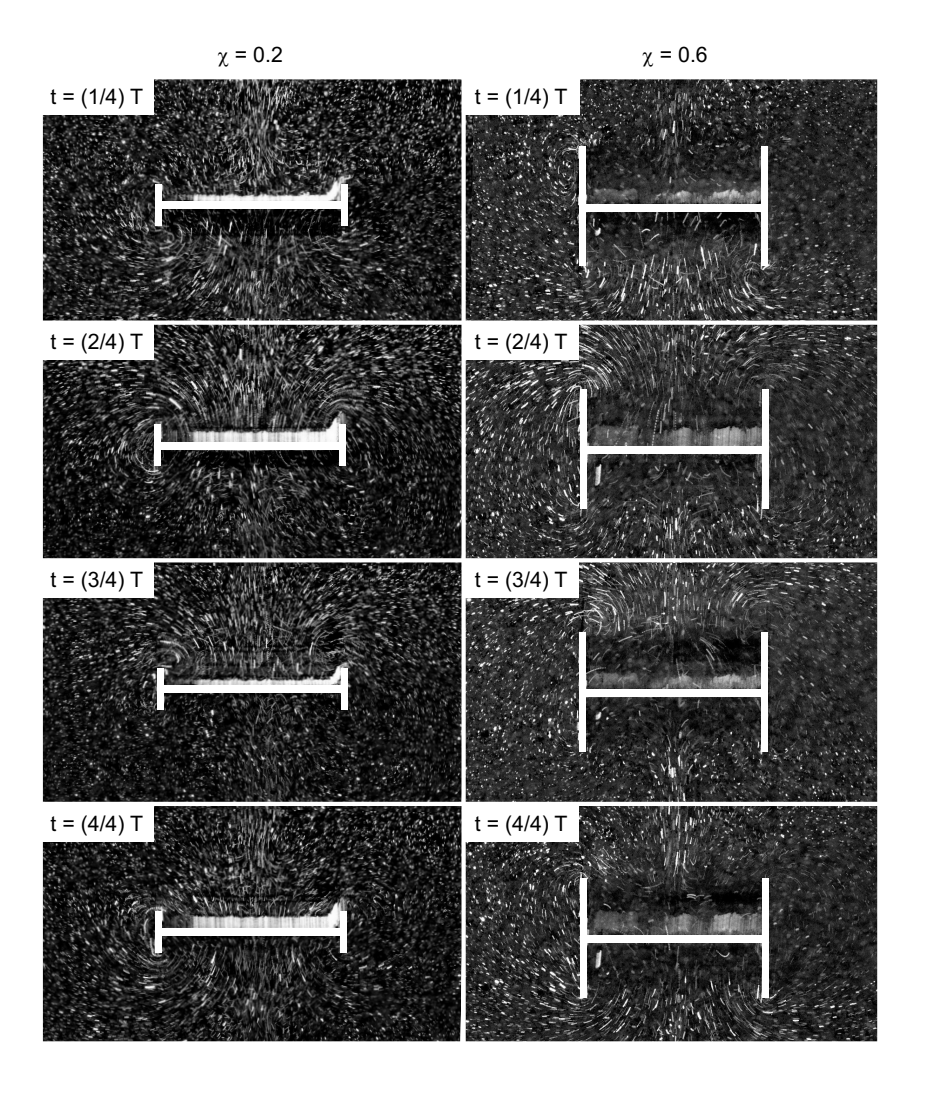


FIG. 9. Particle pathlines with superimposed streamlines at four instants of time in one oscillation cycle of regime C for $\beta = 500$, $\epsilon = 0.1$, and $\chi = 0.2$ (left column) and 0.6 (right column).

PLEASE CITE THIS ARTICLE AS DOI: 10.1063/5.0141889

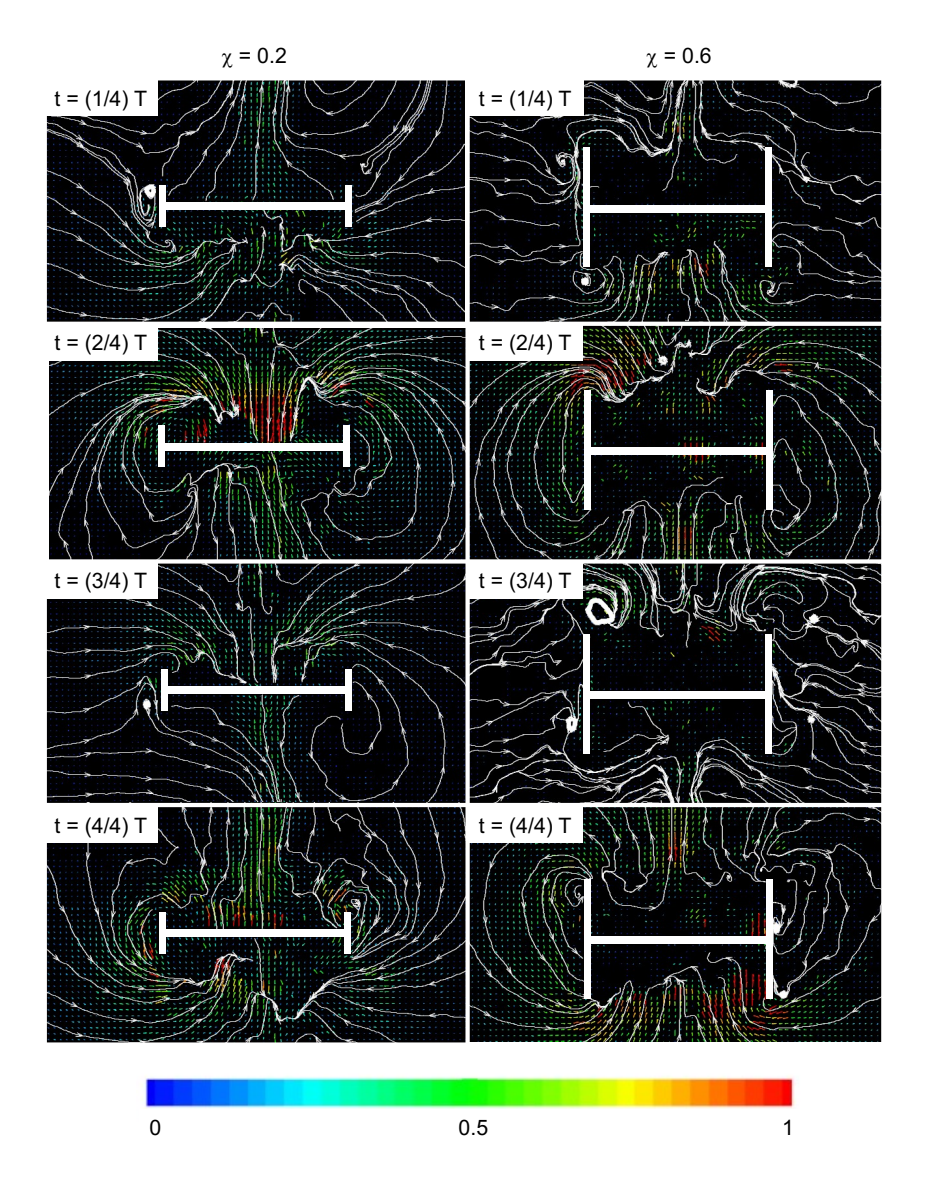


FIG. 10. Instantaneous nondimensional velocity vector fields and superimposed streamlines at four instants of time in one oscillation cycle of regime C for $\beta=500, \epsilon=0.1$, and $\chi=0.2$ (left column) and 0.6 (right column).

PLEASE CITE THIS ARTICLE AS DOI: 10.1063/5.0141889

Accepted to Phys. Fluids 10.1063/5.0141889

that, as compared to the figures for regimes A and B, the panels in Fig. 9 encompass a larger domain around the H-plate to better highlight the larger flow structures that are typical of this hydrodynamic regime. For regime C, the flow around the H-plate mostly retains its symmetry about the x-axis and y-axis. The pathlines and streamlines indicate increased motion in the flow field when compared to regime A and B for all flange ratios. This large motion of the particles adjacent to the flanges results in the formation of two fully developed vortices on the leading and trailing edges of the H-plate, during each upstroke and downstroke half-period. As χ increases, the particle trajectories elongate along the flange size and the leading and trailing edge vortices become more prominent as shown by streamlines at t = T/4 and t = 3T/4, see for example the case $\chi = 0.6$. In this case, the vortices formed during the same half-stroke at the leading and trailing tips of the H-plate do not display significant interaction due to this spatial separation. The vortex interaction dynamics and its dependence on flange size will be addressed more in detail in the next section. It can however be observed that, as the flange size increases, the angle formed between both the leading and trailing flanges and the tangent to the streamline originating from them becomes progressively more acute. Qualitatively similar phenomena were also reported in Ref. 50 for an oscillating disk with varying thickness.

C. Vortex-vortex and vortex-structure interactions

To gain a better understanding of the effect of the flange size on vortex formation and evolution, we present in Fig. 11 different vorticity patterns pertaining to regime C for different flange ratios. The figure consists of superimposed experimental images, constructed the same way as in Figs. 5, 7, and 9, taken at the end of first quarter of one cycle of oscillation for $\beta=500$ and $\epsilon=0.088$, for three different H-plates with $\chi=0.1,\,0.4$, and 0.6, respectively. For ease of illustration, the bottom panels of this figure display cartoon sketches of the streamlines determined from the top panels. Note that the three plates as displayed are subject to the same displacement and velocity and, as a consequence, all vortices shed at the leading edge, captured in the figure, are approximately of the same characteristic size. We posit that the different evolution displayed in the three panels depends on whether the separated flow at the leading edge can reattach to the external side of the flange and on the location of the reattachment point. This phenomenon has also significant impact on the

PLEASE CITE THIS ARTICLE AS DOI: 10.1063/5.0141889

Accepted to Phys. Fluids 10.1063/5.0141889

hydrodynamic forces experienced by the plate.

Specifically, for small flange size, the vortex formations in Fig. 11(a) are reminiscent of those generated by flat plates in our previous work⁴¹. The vortex size is larger than the flange size and there is no reattachment point on the structure. The flow is redirected to the suction region where its energy is eventually dissipated, as evidenced by two conspicuous vortices indicated by the red arrows in the top panel. No significant shedding is observed at the trailing edge, although the leading edge vortex is transported in the vicinity of the trailing tip. In contrast, in Fig. 11(b) for $\chi = 0.4$, the leading edge vortex size becomes comparable with the flange size. The flow is there seen to reattach in proximity of the trailing tip of the flange, leaving behind the leading edge vortex a segment of flange which is largely shielded from shear stresses. We also observe the existence of a different vortex pair on the trailing edge, as indicated by blue arrows in the top panel. Shedding of this pair occurs because the flow is reattached at or before the tip. The separated flows from each edge are seen to interact with each other and form a structure whose characteristic size spans the entire outer edge of the flange, a circumstance that was denoted as "interactive vortex shedding" in other works 50,52,54 . Finally, in Fig. 11(c) for $\chi = 0.6$, the vortex sizes are significantly smaller than the flange size. Reattachment occurs well within the flange length, leaving a substantial fraction of the flange experiencing shear stress. The vortices on the

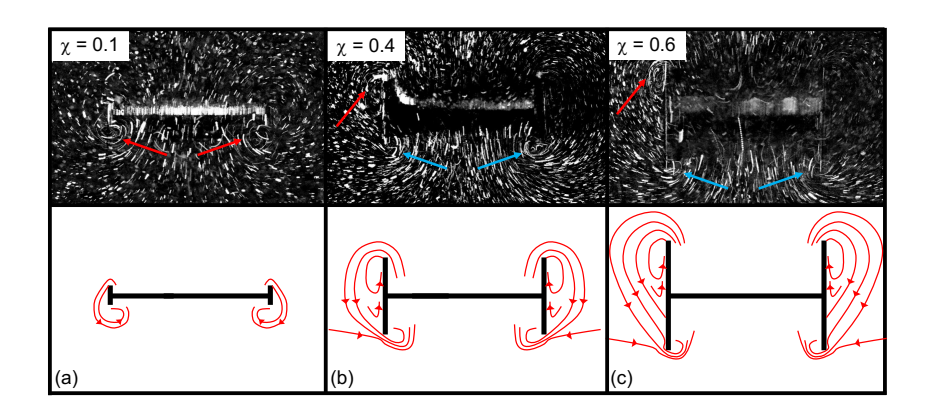


FIG. 11. Top: Particle pathlines at t=(1/4)T for $\beta=500, \epsilon=0.088$. Arrows indicate shed vortices. Bottom: Cartoon representation of the flow structures observed for (a) $\chi=0.1$, (b) $\chi=0.4$, and (c) $\chi=0.6$.

PLEASE CITE THIS ARTICLE AS DOI: 10.1063/5.0141889

Accepted to Phys. Fluids 10.1063/5.0141889

leading and trailing edges, indicated via red and blue arrows in the top panel, respectively, are shed independently from each other and do not significantly interact with each other.

A quantitative representation of the vortical structures associated to regime C is demonstrated in Fig. 12, which consists of vorticity ζ contours of H-plates for $\beta=900, \epsilon=0.12$ for all flange ratios, including a flat plate with $\chi=0$. Flange ratio increases from top to bottom in the figure. Vorticity is calculated as $\zeta=\partial v/\partial x-\partial u/\partial y$, and represents the out-of-plane component of the vorticity vector $\mathbf{\Omega}=\nabla\times\mathbf{u}$. Snapshots are captured at five instants during a cycle, that is, at t=0, t=T/4, t=2T/4, t=3T/4, and t=T. The flow fields pertaining to all flange ratios attain a similar maximum vorticity magnitude over one cycle of an oscillation.

The effect of the flanges can be seen for $\chi=0.1$ in Fig. 12, as two different vortices on the leading and trailing edges are observed to merge. Here, the leading edge vortex formed on the outer side of the flange and the trailing edge vortex formed around the trailing edge are located very close to each other. This case is similar to interactive vortex shedding discussed above for Fig. 11(b). In previous work from our group⁵⁴, we showed that this regime hinders vortex shedding, hence leading to reduction of nonlinear hydrodynamic damping exerted on the H-plate.

Increasing the flange ratio to $\chi=0.2$ results in a transition to the independent vortex shedding seen in Fig. 11(c). Quantitative PIV data reveal that the leading edge vortex is weaker than the trailing vortex at the instants t=2T/4 and t=T. Indeed, for larger flange ratios such as $\chi=0.3$ and beyond, we observe that the a trailing edge vortex is prominent at t=T/4 and t=3T/4 while leading edge vortices cannot be clearly identified, within the adopted vorticity scale. Further increasing the flange ratio leads to further separation of the vortices, without significant changes in qualitative and quantitative results.

At the instants t = T/4 and t = 3T/4 in Fig. 12, where the plate velocity crosses zero and changes sign, for selected flange sizes greater than $\chi = 0.2$, it is possible to observe the permanence of trailing edge vortices. These are not present for the case of smaller flanges. This indicates that the time scales over which leading and trailing edge vortices dissipate are affected by the flange size. In addition, the experimental results, although with the limited resolution available, suggest that the leading and trailing edge vortices occur at slightly different locations in the vicinity of the tip plates. A similar result is observed, for flat plates with different thicknesses oscillating at large β , in Ref. 53, where the x-component

PLEASE CITE THIS ARTICLE AS DOI: 10.1063/5.0141889

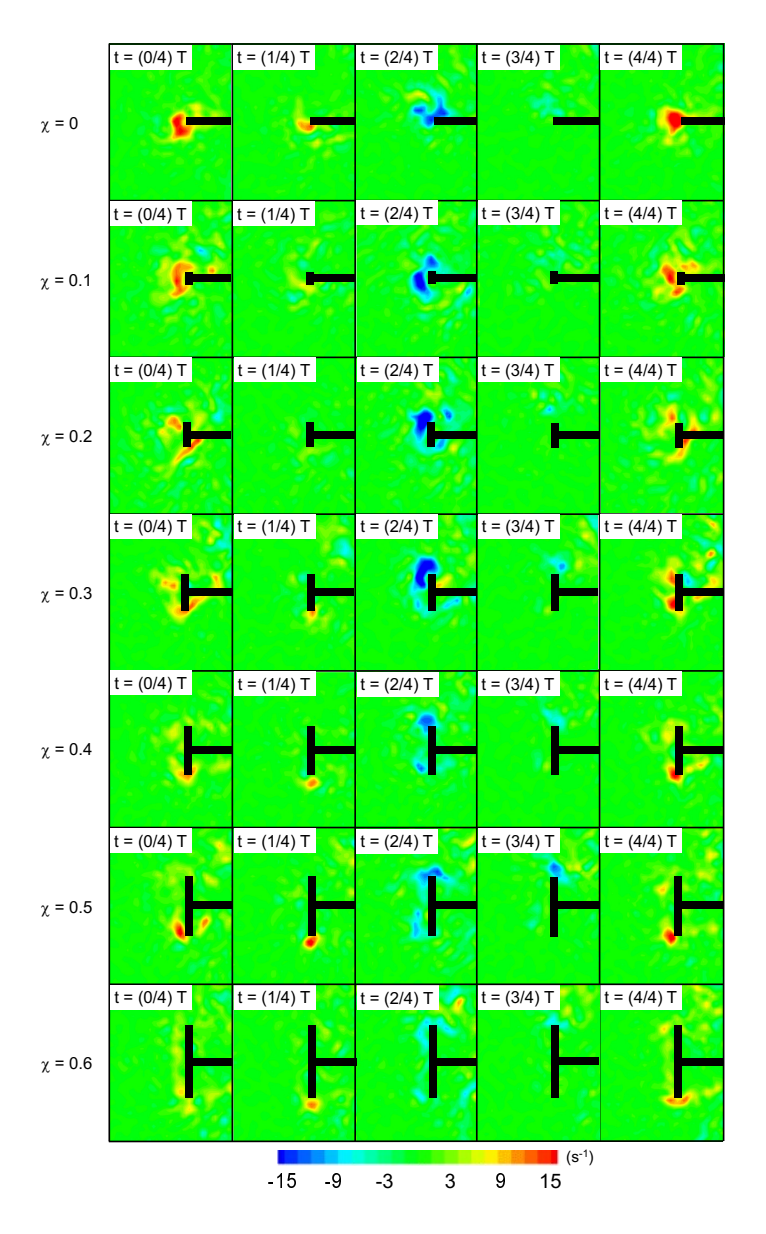


FIG. 12. Instantaneous vorticity patterns of the H-plates at $\beta = 900, \epsilon = 0.12$. Flange ratios from $\chi = 0$ (flat plate for comparison) to $\chi = 0.6$ increase top to bottom.

PLEASE CITE THIS ARTICLE AS DOI: 10.1063/5.0141889

Accepted to Phys. Fluids 10.1063/5.0141889

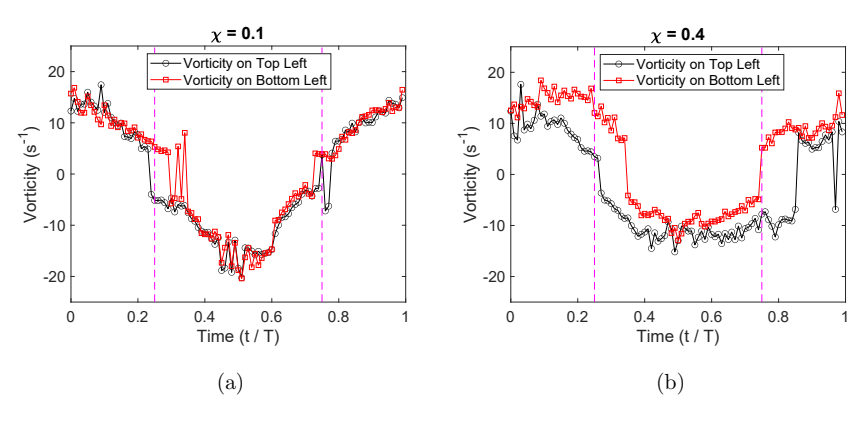


FIG. 13. Time history of vorticity of top and bottom edge of the left side of the plate at $\beta = 900, \epsilon = 0.12$, for (a) $\chi = 0.1$ and (b) 0.4, respectively.

of the pressure, responsible for vortex formation, is reduced for higher aspect ratio cases. This result translates to our study since the presence of flanges provides a qualitatively comparable effect.

These observations motivate us to investigate the behavior of this vortex pair by following the method suggested in Ref. 53, by monitoring the time history of the vorticity in one period of oscillation. Specifically, we search for maximum and minimum vorticity values in two moving square areas in the half plane $x \leq 0$, of extent $1.5b \times 1.5b$ located at $y \geq \delta(t)$ for the vortices at the bottom left of the H-plate. After qualitative verification, we plot their time histories. In some cases, a vortex from a previous quarter period survives in the next one and two opposite vortices can be found in one region of interest for a fraction of the oscillation period. In these instances, we compare the evolution of the two vortices and display the magnitude of the stronger one. Results are shown in Figs. 13(a) and (b), for $\chi=0.1$ and 0.4 respectively, for oscillations at $\beta=900$ and $\epsilon=0.12$. Here, we classify the vortices based on their location as top (y>0) and bottom (y<0) on the left (x<0) side of the H-plate, referring to a prototypical flow field such as those in Fig. 12. Vertical dashed lines in the figure track the instants of plate velocity reversals at t=1/4T and t=3/4T, and therefore the approximate switching times when the leading edge vortex becomes the trailing edge vortex, and vice versa.

The first result is the phase lag between the dissipation of the vortices on top and bottom of the flanges. The lag suggests that the leading edges vortex dissipates more quickly than

PLEASE CITE THIS ARTICLE AS DOI: 10.1063/5.0141889

Accepted to Phys. Fluids 10.1063/5.0141889

the trailing edge vortex, for both short and long flange cases. The physical mechanism for this effect should be sought in the proximity of the trailing edge vortex to the suction side, and in its intense interaction with it. Specifically, the leading edge vortex (top left for t < T/4, bottom left for T/4 < t < 3T/4) dissipates as soon as the direction of the oscillation changes (dashed lines). However, the trailing edge vortex (bottom left for t < T/4) lasts beyond the velocity reversal and its intensity remains larger than that of the new developing leading edge vortex. The permanence of the trailing edge vortex is longer for the larger flange ratio, whereas the leading edge vortex dissipates approximately at the same time for both flange ratios. Moreover, the leading and trailing vortices display similar vorticity for $\chi = 0.1$ whereas the leading edge vortex has smaller vorticity magnitude than the trailing edge vortex for $\chi = 0.4$. This is indicated by the repeated "jumps" of the vorticity value in the general switching region. It is likely that two vortices attain similar vorticity magnitudes for the "interactive vortex shedding" regime. In contrast, the leading and trailing edge vortices possess different vorticity magnitudes for non-interactive shedding.

D. Estimation of hydrodynamic forces

To support our conclusions on the role of vortex dynamics on the hydrodynamic forces on the H-plates, we use the PIV velocity fields to extract time histories of these force data. To estimate these forces, we apply the "Flux Equation" formula provided in Refs. 75 and 85 which, with the current nomenclature, reads:

$$\mathbf{F}(t) = \rho \oint_{C_F} \hat{\mathbf{n}} \cdot \mathbf{G} \, \mathrm{d}\ell + \rho \mathcal{S} \ddot{\delta}(t) \mathbf{e_2}$$
 (2)

Here, F(t) is the estimated force vector (per unit length) on the H-plate at time t during the oscillation, $\delta(t)$ is the prescribed rigid body displacement of the H-plate defined above, \mathcal{S} is the cross sectional area of the H-plate, C_F denotes the fixed outer boundary of the control area, see Fig. 1(c), $\hat{\boldsymbol{n}}$ is the unit outer normal vector to the fluid domain boundary, and \boldsymbol{G} is a tensor defined as⁴¹

$$\mathbf{G} = \left(\frac{1}{2}u^{2}\mathbf{I} - \boldsymbol{u}\boldsymbol{u} - \boldsymbol{u}(\boldsymbol{x} \times \boldsymbol{\Omega}) + \boldsymbol{\Omega}(\boldsymbol{x} \times \boldsymbol{u})\right) - \left[\left(\boldsymbol{x} \cdot \frac{\partial \boldsymbol{u}}{\partial t}\right)\mathbf{I} - \boldsymbol{x}\frac{\partial \boldsymbol{u}}{\partial t} + \frac{\partial \boldsymbol{u}}{\partial t}\boldsymbol{x}\right] + 2\mu\left[\boldsymbol{x} \cdot (\nabla \cdot \mathbf{D})\mathbf{I} - \boldsymbol{x}(\nabla \cdot \mathbf{D})\right] + 2\mu\mathbf{D} \quad (3)$$

PLEASE CITE THIS ARTICLE AS DOI: 10.1063/5.0141889

Accepted to Phys. Fluids 10.1063/5.0141889

where $\Omega = \zeta e_3$ is the vorticity vector with e_3 the unit vector in the direction of the z-axis. Here, \mathbf{I} is the identity tensor and \mathbf{D} is the symmetric part of the velocity gradient tensor, that is, $\mathbf{D} = \frac{1}{2}(\nabla \boldsymbol{u} + \nabla \boldsymbol{u}^T)$, where $(\cdot)^T$ denotes transpose. In our notation above, consistently with Ref. 75, juxtaposition of two vectors denotes their tensor product so that the (i, j)-th component of the tensor ab is a_ib_j . Similarly, the j-th component of the divergence $\nabla \cdot \mathbf{D}$ of tensor \mathbf{D} is defined as $\partial D_{ij}/\partial x_i$. Once the forces are estimated according to Eq. (2), the component in the direction of motion can be isolated as $F_y(t) = F(t) \cdot e_2$. We then calculate the fundamental harmonic of the time history of this force component, assuming periodicity of period $T = 2\pi/\omega$, via a single term Fourier series over a given identification time window, such that $F_y(t) = a_1 \cos(\omega t) + b_1 \sin(\omega t)$. Finally, we estimate the hydrodynamic function $\Theta(\beta, \epsilon, \chi)$ from the implicit relations⁵⁴:

$$\Theta(\beta, \epsilon, \chi) = (b_1 + ia_1)/[\rho(\pi/4)b^2\omega^2 A] \tag{4}$$

where the coefficient in square brackets is a scaling factor that has the physical meaning of mass times acceleration (phasor) of a cylinder of fluid of diameter equal to b (the dominant structure dimension) oscillating as the structure. The physical meaning of the Fourier coefficients b_1 and a_1 is therefore that of real and imaginary part of the hydrodynamic function Θ , which in turn correspond to the terms "added mass effect" and "hydrodynamic damping effect", respectively^{43,86}. In other words, these terms indicate forces in phase with the acceleration or the velocity of the structure, respectively. In Fig. 14, we present results of the hydrodynamic function estimation using Eq. (4) to highlight the influence on $\text{Re}[\Theta]$ and $-\text{Im}[\Theta]$ of the flange ratio χ . Representative data are provided for $\epsilon = 0.12$ for values of β equal to 300, 500, 900, and 1200.

Experimental results in Fig. 14(a) show that the added mass effect $\text{Re}[\Theta]$ increases approximately with a linear trend with increasing flange ratio. In other words, as the flange size increases, the H-plate entrains a larger amount of fluid within its oscillatory motion, thus increasing the inertia forces. On the other hand, results on $-\text{Im}[\Theta]$ show a more complex nonmonotonic dependence on χ . The hydrodynamic damping attains its maximum value of approximately 0.4 at relatively low $\beta=300$ and $\chi=0.1$, where vortex shedding exhibits similar characteristics to those of a flat plate with $\chi=0$. Damping decreases as the flange size increases, for all β values presented, in the neighborhood of the interactive vortex shedding regime. Both $\text{Re}[\Theta]$ and $-\text{Im}[\Theta]$ exhibit qualitatively similar behavior to

PLEASE CITE THIS ARTICLE AS DOI: 10.1063/5.0141889

Accepted to Phys. Fluids 10.1063/5.0141889

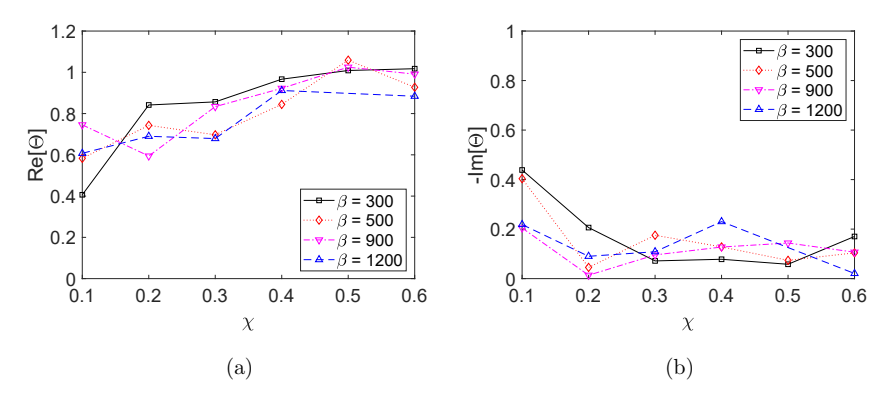


FIG. 14. Behavior of the fundamental harmonics of the hydrodynamic force as described via the complex hydrodynamic function Θ . Added mass is $Re[\Theta]$ in (a) and hydrodynamic damping is $-Im[\Theta]$ in (b), at $\epsilon = 0.12$, $\beta = 300, 500, 900$, and 1200.

what described in Ref. 54. We note, however, some discrepancies in the quantitative values of the numerical calculation⁵⁴ and of our present experimental results. The cause for these discrepancies could possibly be ascribed to potential 3D effects not captured in the simulations, as well as to experimental limitations stemming from inconsistent illumination inside and on the right side of the H-plate.

E. Steady streaming

The instantaneous streamlines displayed in Figs. 6, 8, and 10 provide initial evidence for steady streaming. Although steady streaming is a classic result in the flow generated by periodic oscillations of circular cylinders⁶¹, investigation in the context of H-plates, and the study of the potential effect of flange ratio on the characteristics of streaming, has not been discussed before. Qualitatively, in our experiments, the streamlines exhibit structure similar to those of oscillating cylinders^{61,73}. For instance, in Fig. 10, the instantaneous streamlines around the midpoint (x=0) of the H-plates are aligned along the vertical direction, that is, in the same direction of transverse oscillations. In this case, the PIV seeding particles are seen to move away from the plate along the y-axis in both directions. Vice versa, at the instants t=T/4 and t=3T/4, the streamlines are aligned in the horizontal direction, and the particles are moving towards the plate from the left and right sides of the frame.

PLEASE CITE THIS ARTICLE AS DOI: 10.1063/5.0141889

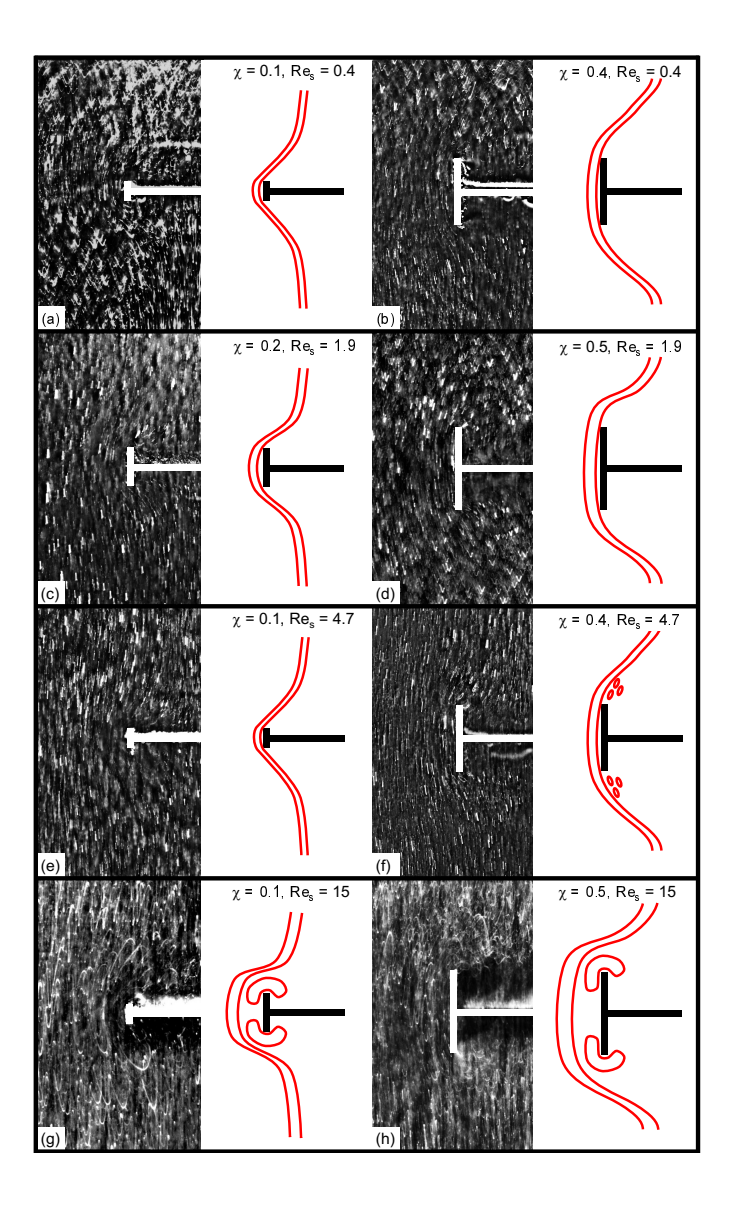


FIG. 15. Average particle pathlines (on the left of each panel) and sketch to aid visual interpretation (on the right of panel) over one oscillation cycle. In (a): $\beta=160, \epsilon=0.02$; in (b): $\beta=160, \epsilon=0.02$; in (c): $\beta=700, \epsilon=0.021$; in (d): $\beta=900, \epsilon=0.018$; in (e): $\beta=1200, \epsilon=0.025$; in (f): $\beta=1200, \epsilon=0.025$; in (g): $\beta=100, \epsilon=0.155$; in (h): $\beta=100, \epsilon=0.155$.

PLEASE CITE THIS ARTICLE AS DOI: 10.1063/5.0141889

Accepted to Phys. Fluids 10.1063/5.0141889

To develop insight on the steady streaming for our problem, we present in Fig. 15 the time-averaged flow patterns (on the left of each panel) and idealized streamlines (on the right of each panel) over one period of oscillation. The time-averaged pathlines on the left panels are constructed differently from those shown in Figs. 5, 7, and 9, as we keep the position of the H-plate fixed in the field of view, rather than fixing the camera position. This approach is inspired by the classical visualizations of steady streaming in the monographs by Schlichting⁶¹ and by Van Dyke⁸⁷ which emphasize the fluid motion relative to the oscillating body.

In Fig. 15, we present the analysis of the flow generated by distinct H-plates with varying flange ratio. For each, we show qualitatively different conditions based on the oscillating boundary layer classification for oscillating cylinders developed by Stuart⁷⁴. Therein, streaming is classified based on the so called steady streaming Reynolds number Re_s defined, using the nomenclature of the present paper, as $Re_s = 2\pi\epsilon^2\beta$. In Ref. 74, it is observed that for $Re_s \leq 1$, the flow field is governed by the Stokes equation and the boundary layer generated by the oscillation is called "Stokes boundary layer". For $Re_s \geq 1$, a secondary boundary layer is present for oscillating cylinders^{68,88}, which is referred to as recirculation cell or streaming cell. Although Re_s is expected to control the characteristics of the steady streaming, we don't anticipate that $Re_s = 1$ indicates the transition in the case of the H-plate.

For the present case, we show in Fig. 15 different experimental conditions, covering a range of steady streaming Reynolds number of Re_s = 0.4, 1.9, 4.7, and 15. For each of these values, a small and large flange ratio case is displayed. Specifically, in (a): $\chi=0.1$, $\beta=160$, and $\epsilon=0.02$; in (b): $\chi=0.4$, $\beta=160$, and $\epsilon=0.02$; in (c): $\chi=0.2$, $\beta=700$, and $\epsilon=0.021$; in (d): $\chi=0.5$, $\beta=900$, and $\epsilon=0.018$; in (e): $\chi=0.1$, $\beta=1200$, and $\epsilon=0.025$; in (f): $\chi=0.4$, $\beta=1200$, and $\epsilon=0.025$; in (g): $\chi=0.1$, $\chi=0.1$,

In Figs. 15(a) and (b), we present a moderately low steady streaming Reynolds number case, with $\mathrm{Re_s}=0.4$. The pathlines indicate substantial vertical motion as a result of the oscillation. At the top and bottom of the H-plates, we observe diagonal motion of particles towards the suction side for each up and down stroke. The particles in these regions exhibit paths resembling the letter "V", indicating the presence of additional horizontal motion caused by the pressure gradient. These structures are similar to those observed in Ref. 73 for particles in the neighborhood of an oscillating cylinder. We note, however,

This is the author's peer reviewed, accepted manuscript. However, the online version of record will be different from this version once it has been copyedited and typeset PLEASE CITE THIS ARTICLE AS DOI: 10.1063/5.0141889

Accepted to Phys. Fluids 10.1063/5.0141889

that in Ref. 73 the trajectories pertain to multiple oscillation cycles for absolute velocities, and therefore the "zig-zag like" traces defined therein look more complicated that the "V" observed here. While these trajectories hint to comparable magnitudes of the steady and unsteady components of the flow velocity⁷³, the horizontal motion seen here may also be in part an experimental consequence of the overall low velocities in the field, comparable to background velocity due to noise. Importantly, increasing the flange ratio does not result in major qualitatively changes in the flow patterns for this case. The qualitative aspects of the flow remain the same in Figs. 15(c) and (d), where the steady streaming Reynolds number is of the order of the critical value of steady streaming for oscillating cylinder. The flow in these panels further demonstrates that the parameter β and ϵ do not independently affect steady streaming, as they are substantially different between the case in Figs. 15(c) and (d). Similarly, no qualitative difference seems to be elicited by the different flange ratios. Vice versa, for the case in Figs. 15(e) and (f) with $Re_s = 4.7$, the flange ratio appears to affect the details of the flow. In the neighborhood of the flanges, we observe illuminated particles performing closed loop periodic orbits that are likely happening inside the primary streaming cell. The size of this cell is of the order of the flange size. By using the scaling arguments in Ref. 68, and originally developed by Stuart⁷⁴, the thickness of the primary cell for the current value of β is predicted to be approximately half the thickness of the flange, as confirmed visually. From our experiments, due to the challenging size of the cell (approximately 0.4 mm), we are not able to fully describe the dynamics of the flow along the flange; however, it looks like there may be two separate primary cells in the neighborhood of the flange tips, rather than one as in the circular cylinder case.

We should note that in the classical definition of Re_s , the characteristic length scale for the oscillating cylinder is the radius. In this work, we are using as characteristic length the whole width of the H-plate, that in some sense would be equivalent to the diameter of a cylinder. If a steady streaming Reynolds number were to be calculated based on the diameter, the critical transition should be observed at $Re_s \approx 4$. This does not appear to be the case for the H-plates, for which we are not able to pinpoint a critical Re_s for the transition.

However, a secondary streaming cell can be easily identified by selecting a moderately large steady streaming Reynolds number case, as presented in Figs. 15(g) and (h). Here, the H-plates oscillate at $\mathrm{Re_s}=15$. Particles retain substantial vertical motion for this case as

PLEASE CITE THIS ARTICLE AS DOI: 10.1063/5.0141889

Accepted to Phys. Fluids 10.1063/5.0141889

well. The visualizations strongly indicate the presence of a secondary boundary layer around the flanges, revealed by the curvature of pathlines in the vicinity of the flanges. We note that this boundary layer corresponds to a vortex shedding regime and the vortices are shed inside the secondary boundary layer. As explained in Ref. 68, the Reynolds stress decreases exponentially further away from the flanges and the flow around the plate drives the steady streaming outside of the boundary layer. The streamlines outside of the boundary layers show a curvature with a smaller radius around the streaming cell, as compared to the other cases in the same figure. Although we are unable at this time to pinpoint the incipient appearance of the secondary boundary layer to a specific value of Res, it is interesting to note that the same qualitative critical streaming Reynolds number governs the flow for the case of the H-plates, as it does for the case of a circular cylinder.

Motivated by the variety of structures observed in the average particle pathlines in Fig. 15, we ask the question whether pathlines with the same Re_s might differ qualitatively depending on the particular hydrodynamic regime of the flow and on the characteristics of vortex shedding, as also observed in Ref. 89. To investigate these potential differences, we present in Fig. 16 the average pathlines for three different regimes, by keeping χ and Re_s fixed at 0.3 and 15, respectively. By using the phase diagram information in Fig. 2 for $\chi = 0.3$, regime A in panel (a) is selected from $\beta = 1800$ and $\epsilon = 0.036$, regime B in panel (b) is selected from $\beta = 700$ and $\epsilon = 0.058$, and regime C in panel (c) is selected from $\beta = 100$ and $\epsilon = 0.154$. We remark that the pathlines in Fig. 16 are constructed with the relative fluid motion (using the "fixed H-plate" approach in this section) and therefore look different from the pathlines exemplified in Fig. 3, which are constructed from the absolute velocity fields (using the "fixed camera" approach). Because of the moderately large value of Res, the following discussion focuses on the characteristics of the secondary boundary layer, although the primary boundary layer could still be identified in the visualizations.

In regime A, occurring for high β and low ϵ , in Fig. 16(a), the average pattern exhibits closed loop periodic orbits around the flanges (more apparent on the left side). These are different structures than those mentioned above in Fig. 15. Switching to regime B, for intermediate β and ϵ , results in larger closed loops and corresponds to the relative velocity version of the "figure-8" patterns. Finally, in regime C, occurring for low β and high ϵ , pathlines display open in proximity of the flange tips. Consistently with the scaling predictions in Ref. 68 for the thickness of the secondary boundary layer which should decrease

PLEASE CITE THIS ARTICLE AS DOI: 10.1063/5.0141889

Accepted to Phys. Fluids 10.1063/5.0141889

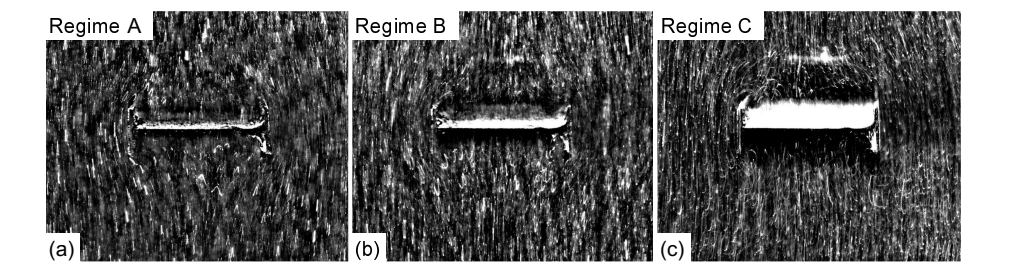


FIG. 16. Average particle pathlines for different hydrodynamic regimes, for Re_s = 15 and $\chi = 0.3$. In (a): regime A with $\beta = 1800$, $\epsilon = 0.036$; in (b): regime B with $\beta = 700$, $\epsilon = 0.058$; in (c): regime C with $\beta = 100$, $\epsilon = 0.154$.

as β increases, the thickness of the boundary layer seems to decrease from left to right, from regime A to regime C.

For the cases discussed, the flange ratio does not seem to play a major role in triggering this transition, as the flow fields are comparable between moderately small and moderately large χ values. However, the quantitative details of the flow are affected by χ . To understand the dynamics of the flow in the vicinity of the streaming cells in a quantitative perspective, we consider a square control volume centered on the H-plate, with sides equal to 1.5b. We conduct a Fourier analysis on the space averaged fluxes $q_s(t)$ across the top and bottom boundary of this control volume, as derived from Eq. (1), to assess periodicity characteristics of this flow. We present in Fig. 17 two cases at moderately large Re_s, both with $\epsilon = 0.12$, for $\beta = 300$ (Re_s = 27) in panel (a) and $\beta = 1200$ (Re_s = 109) in panel (b). We select the same ϵ in the two cases since the size of the secondary streaming cell is only affected by the value of β , see Ref. 68.

In the figure, we present the magnitude of the first three harmonics of the normalized vertical fluxes as a function of flange ratio. The first harmonic is consistently the dominant component and approximately one order of magnitude larger than the second and third harmonics. The first harmonic is seen to generally increase in an approximately linear fashion with χ for the two values of β shown. The increase in average flux can be explained by considering the increasing boundary layer size in the y-direction as the flange ratio increases and by recalling that the boundary layer is the driving mechanism for the outer flow of the streaming cell⁶⁸. Interestingly, the slope of the linear trend decreases for higher β . In

PLEASE CITE THIS ARTICLE AS DOI: 10.1063/5.0141889

Accepted to Phys. Fluids 10.1063/5.0141889

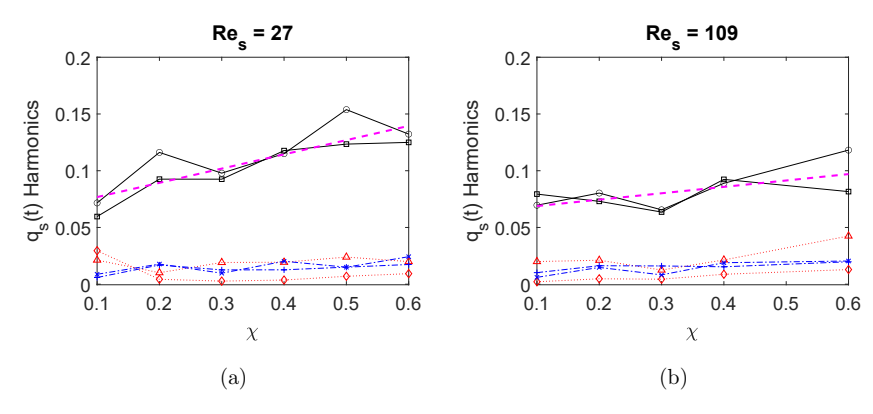


FIG. 17. Magnitudes of the first three harmonics of the Fourier analysis of normalized fluxes along vertical direction at the top and bottom boundaries. First harmonic: \bigcirc top and \square bottom. Second harmonic: \triangle top and \diamondsuit bottom. Third harmonic: + top and \times bottom. Line fit to aid visual interpretation for the first harmonics: dashed line. In (a): $\beta = 300$ and $\epsilon = 0.12$. In (b): $\beta = 1200$ and $\epsilon = 0.12$.

Ref. 68, the thickness of the streaming cell is associated with β^{-1} , such that it decreases with increasing β . As this boundary layer thickness decreases, the flow at a sufficient distance away, outside of it, is less and less affected by the geometric details of the structure inside the layer. At the same time, the analysis of the space- and time-averaged fluxes yields non-zero mean values, i.e. "zero"-th harmonics, whose magnitude is comparable to that of the first harmonic; however, it does not display a definite trend as a function of the flange ratio.

IV. CONCLUSIONS

In this work, we investigated quantitatively and qualitatively the flow dynamics of an oscillating H-plate immersed in a stationary, incompressible and Newtonian fluid environment. In addition to the governing parameters used in the literature on oscillating flat plates, that is, nondimensional frequency β and amplitude of oscillation ϵ , a third parameter, the flange ratio χ , establishes the geometry of the plate. We performed a broad experimental campaign based on particle image velocimetry to demonstrate both quantitative and qualitative flow physics characteristics, including pathlines, vorticity contours, vorticity time history, and steady streaming, and their dependence on the three governing parameters.

PLEASE CITE THIS ARTICLE AS DOI: 10.1063/5.0141889

Accepted to Phys. Fluids 10.1063/5.0141889

We identified and presented qualitatively distinct hydrodynamic regimes in novel phase planes and discussed their dependence on flange ratios. Based on qualitative aspects of vortex formation, we identified three primary regimes occurring for most flange ratios. In the first regime, indicated as Regime A, the flow is linear and governed by the unsteady Stokes equations. As frequency and amplitude increase, the flow exhibits nonlinearities, defining regime B. Here, the flanges shape the flow, as vortex formation occurs on the pairs of leading and trailing edges, resulting in unique and distinctive flow physics. Finally, for regime C, in which vortex shedding is the dominant transport mechanism, the effect of the flange ratio is to modify the vortex dynamics, for example by transitioning from one shed vortex to two shed vortices on the leading and trailing edges. By analyzing the hydrodynamic regime phase planes, the pathlines, and the vorticity contours, we identified conditions in which these vortices have strong or weak mutual interactions, and correlated these interactions with the flange ratios. Strong interaction of the leading and trailing edge vortices was associated to circumstances in which minimum hydrodynamic damping is achieved, consistently with previous findings⁵⁴. Key results include the delayed regime transitions as a function of the flange ratio, the vortex shedding attenuation with increasing χ , and the modulation of vortex dynamics time scales.

The interplay of the three governing parameters is also central to the characteristics of steady streaming for our system. We show that steady streaming of H-plates can be approached in terms of the streaming Reynolds number, that was originally defined for circular cylinders. Specifically, for relatively small Re_s , we observed the presence of a Stokes layer. Vice versa, for relatively large Re_s , we identified a secondary boundary layer or streaming cell. Streaming is studied quantitatively, by analyzing the harmonic content of the space-average flux in the vicinity of the H-plate. We found that the fundamental harmonics of the vertical streaming flux are dominant and increase with increasing flange ratio, while this increase seems to be less sensitive for higher β values.

We believe that this works provides fundamental insight to the flow physics of oscillating H-plates and can shed light on the effect of the governing parameters on vortex-vortex and vortex-structure interactions shaping the flow. While the primary goal of this study is to explore the fundamental physics of this relatively untapped system, we envision practical applications for the theoretical findings of this paper. The knowledge of how the flanges affect the vortex formation and shedding, and in particular on their delaying effects, could be useful

PLEASE CITE THIS ARTICLE AS DOI: 10.1063/5.0141889

Accepted to Phys. Fluids 10.1063/5.0141889

in the design of vibrating systems, either for structural applications, such as suspension H-shaped bridges, or for mechatronics applications, such as fluid-based energy harvesters. In both exemplary cases, the intended dynamics of the system is dependent on careful control of the flow energy and of the mechanisms of energy exchange between the flow and the structure. As demonstrated, the presence of the flanges can modify the energy dissipation profile in the vibration process and modulate the hydrodynamic forces in fluid structure interactions. This, in turn, can be leveraged in passive flow control scenarios towards efficient manipulation of fluid energy.

ACKNOWLEDGEMENTS

This material is based in part upon work supported by the National Science Foundation under grant 1847513. The authors thank Ms. Anna Zueva for her help with some of the figures.

AUTHOR DECLARATIONS

Conflict of Interest

The authors have no conflicts to disclose.

Author Contributions

Burak Gulsacan: Conceptualization (supporting); Data curation (lead); Formal analysis (lead); Investigation (lead); Methodology (supporting); Software (equal); Validation (equal); Visualization (equal); Writing - original draft (lead); Writing - review & editing (equal).

Matteo Aureli: Conceptualization (lead); Data curation (supporting); Formal analysis (supporting); Funding acquisition (lead); Investigation (supporting); Methodology (lead); Project administration (lead); Resources (lead); Software (equal); Supervision (lead); Validation (equal); Visualization (equal); Writing - original draft (supporting); Writing - review & editing (equal).

PLEASE CITE THIS ARTICLE AS DOI: 10.1063/5.0141889

Accepted to Phys. Fluids 10.1063/5.0141889

DATA AVAILABILITY

The data that support the findings of this study are available from the corresponding author upon reasonable request.

REFERENCES

- ¹G. G. Stokes, "On the effect of the internal friction of fluids on the motion of pendulums," Transactions of the Cambridge Philosophical Society, vol. 9, pp. 8–106, 1851.
- ²N. Riley, "Oscillating viscous flows," *Mathematika*, vol. 12, no. 2, pp. 161–175, 1965.
- ³J. H. Gerrard, "The mechanics of the formation region of vortices behind bluff bodies," Journal of Fluid Mechanics, vol. 25, no. 02, pp. 401–413, 1966.
- ⁴S. Singh, Forces on bodies in an oscillatory flow. PhD thesis, Imperial College, University of London, 1979.
- ⁵M. Tatsuno and P. W. Bearman, "A visual study of the flow around an oscillating circular cylinder at low Keulegan-Carpenter numbers and low Stokes numbers," *Journal of Fluid Mechanics*, vol. 211, pp. 157–182, 1990.
- ⁶J. R. Zierenberg, H. Fujioka, K. E. Cook, and J. B. Grotberg, "Pulsatile flow and oxygen transport past cylindrical fiber arrays for an artificial lung: computational and experimental studies," *Journal of Biomechanical Engineering*, vol. 130, no. 3, p. 031019, 2008.
- ⁷F. Zafar and M. Alam, "A low Reynolds number flow and heat transfer topology of a cylinder in a wake," *Physics of Fluids*, vol. 30, no. 8, p. 083603, 2018.
- ⁸D. Choi and H. Park, "Flow around in-line sphere array at moderate Reynolds number," Physics of Fluids, vol. 30, p. 097104, 2018.
- ⁹A. Li, A. Mentzelopoulos, M. S. Triantafyllou, and D. Fan, "Dual-frequency vortex-induced vibrations of long flexible stepped cylinders," *Physics of Fluids*, vol. 34, no. 7, p. 075105, 2022.
- ¹⁰A. Mu, Z. Huang, A. Liu, B. Yang, J. Wang, Y. Qian, and H. Wang, "Bluff body vortex-induced vibration control of floating wind turbines based on a novel intelligent robust control algorithm," *Physics of Fluids*, vol. 34, p. 114103, 2022.
- ¹¹H. Wang, C. Zhao, L. Zeng, M. M. Alam, and H. Tang, "Control of the flow around a finite square cylinder with a flexible plate attached at the free end," *Physics of Fluids*,

PLEASE CITE THIS ARTICLE AS DOI: 10.1063/5.0141889

Accepted to Phys. Fluids 10.1063/5.0141889

vol. 34, p. 027109, 2022.

- ¹²C. Brücker, J. Spatz, and W. Schröder, "Feasability study of wall shear stress imaging using microstructured surfaces with flexible micropillars," *Experiments in Fluids*, vol. 39, pp. 464–474, 2005.
- ¹³T. Manzaneque, V. Ruiz-Díez, J. Hernando-García, E. Wistrela, M. Kucera, U. Schmid, and J. L. Sánchez-Rojas, "Piezoelectric MEMS resonator-based oscillator for density and viscosity sensing," Sensors and Actuators A: Physical, vol. 220, pp. 305–315, 2014.
- ¹⁴T. A. House, V. H. Lieu, and D. T. Schwartz, "A model for inertial particle trapping locations in hydrodynamic tweezers arrays," *Journal of Micromechanics and Microengineering*, vol. 24, no. 4, p. 045019, 2014.
- ¹⁵L. Ma, K. Lin, D. Fan, J. Wang, and M. S. Triantafyllou, "Flexible cylinder flow-induced vibration," *Physics of Fluids*, vol. 34, p. 011302, 2022.
- ¹⁶P. W. Bearman, "Vortex shedding from oscillating bluff bodies," Annual Review of Fluid Mechanics, vol. 16, no. 1, pp. 195–222, 1984.
- ¹⁷C. H. K. Williamson and A. Roshko, "Vortex formation in the wake of an oscillating cylinder," *Journal of Fluids and Structures*, vol. 2, no. 4, pp. 355–381, 1988.
- ¹⁸C. H. K. Williamson, "Sinusoidal flow relative to circular cylinders," *Journal of Fluid Mechanics*, vol. 155, pp. 141–174, 1985.
- ¹⁹K. M. Lam, J. C. Hu, and P. Liu, "Vortex formation processes from an oscillating circular cylinder at high Keulegan-Carpenter numbers," *Physics of Fluids*, vol. 22, no. 1, p. 015105, 2010.
- ²⁰G. H. Keulegan and L. H. Carpenter, "Forces on cylinders and plates in an oscillating fluid," vol. 60, no. 5, pp. 423–440, 1958.
- ²¹R. P. Kanwal, "Vibrations of an elliptic cylinder and a flat plate in a viscous fluid," ZAMM-Journal of Applied Mathematics and Mechanics/Zeitschrift für Angewandte Mathematik und Mechanik, vol. 35, no. 1-2, pp. 17–22, 1955.
- ²²E. O. Tuck, "Calculation of unsteady flows due to small motions of cylinders in a viscous fluid," *Journal of Engineering Mathematics*, vol. 3, no. 1, pp. 29–44, 1969.
- ²³R. A. Bidkar, M. Kimber, A. Raman, A. K. Bajaj, and S. V. Garimella, "Nonlinear aerodynamic damping of sharp-edged flexible beams oscillating at low Keulegan–Carpenter numbers," *Journal of Fluid Mechanics*, vol. 634, pp. 269–289, 2009.

PLEASE CITE THIS ARTICLE AS DOI: 10.1063/5.0141889

- ²⁴M. Aureli and M. Porfiri, "Low frequency and large amplitude oscillations of cantilevers in viscous fluids," *Applied Physics Letters*, vol. 96, no. 16, p. 164102, 2010.
- ²⁵M. Duclercq, D. Broc, and O. Cadot, "Characterization of long time fluctuations of forces exerted on an oscillating circular cylinder at KC=10," *Journal of Fluids and Structures*, vol. 27, no. 4, pp. 596–610, 2011.
- ²⁶M. Aureli, C. Prince, M. Porfiri, and S. D. Peterson, "Energy harvesting from base excitation of ionic polymer metal composites in fluid environments," *Smart materials and Structures*, vol. 19, no. 1, p. 015003, 2009.
- ²⁷A. Erturk and G. Delporte, "Underwater thrust and power generation using flexible piezoelectric composites: an experimental investigation toward self-powered swimmer-sensor platforms," Smart Materials and Structures, vol. 20, no. 12, p. 125013, 2011.
- ²⁸J. A. C. Dias, C. De Marqui, and A. Erturk, "Hybrid piezoelectric-inductive flow energy harvesting and dimensionless electroaeroelastic analysis for scaling," *Applied Physics Letters*, vol. 102, no. 4, p. 044101, 2013.
- ²⁹J. Wu, C. Shu, N. Zhao, and F.-B. Tian, "Numerical study on the power extraction performance of a flapping foil with a flexible tail," *Physics of Fluids*, vol. 27, no. 1, p. 013602, 2015.
- ³⁰H. Hosaka, K. Itao, and S. Kuroda, "Damping characteristics of beam-shaped micro-oscillators," Sensors and Actuators A: Physical, vol. 49, no. 1, pp. 87–95, 1995.
- ³¹C. Castille, I. Dufour, and C. Lucat, "Longitudinal vibration mode of piezoelectric thick-film cantilever-based sensors in liquid media," *Applied Physics Letters*, vol. 96, no. 15, p. 154102, 2010.
- ³²A. Eastman and M. L. Kimber, "Aerodynamic damping of sidewall bounded oscillating cantilevers," *Journal of Fluids and Structures*, vol. 51, pp. 148–160, 2014.
- ³³M. Kimber and S. V. Garimella, "Measurement and prediction of the cooling characteristics of a generalized vibrating piezoelectric fan," *International Journal of Heat and Mass Transfer*, vol. 52, no. 19, pp. 4470–4478, 2009.
- ³⁴J. E. Sader, "Frequency response of cantilever beams immersed in viscous fluids with applications to the atomic force microscope," *Journal of Applied Physics*, vol. 84, no. 1, pp. 64–76, 1998.
- ³⁵R. Cox, F. Josse, S. M. Heinrich, O. Brand, and I. Dufour, "Characteristics of laterally vibrating resonant microcantilevers in viscous liquid media," *Journal of Applied Physics*,

PLEASE CITE THIS ARTICLE AS DOI: 10.1063/5.0141889

Accepted to Phys. Fluids 10.1063/5.0141889

vol. 111, no. 1, p. 014907, 2012.

- ³⁶S. Basak, A. Raman, and S. V. Garimella, "Hydrodynamic loading of microcantilevers vibrating in viscous fluids," *Journal of Applied Physics*, vol. 99, no. 11, p. 114906, 2006.
- ³⁷R. Shihab and R. C. Tung, "Numerical verification of the hydrodynamic reconstruction method for contact resonance atomic force microscopy," AIP Advances, vol. 8, no. 8, p. 085015, 2018.
- ³⁸M. Aureli, V. Kopman, and M. Porfiri, "Free-locomotion of underwater vehicles actuated by ionic polymer metal composites," *IEEE/ASME Transactions on Mechatronics*, vol. 15, no. 4, pp. 603–614, 2010.
- ³⁹L. Yao, C. Hefler, W. Shyy, and H. H. Qiu, "Effects of gradual flexibility and trailing edge shape on propulsive performance of pitching fins," *Physics of Fluids*, vol. 33, no. 7, p. 071910, 2021.
- ⁴⁰A. De Rosis, G. Falcucci, S. Ubertini, and F. Ubertini, "Aeroelastic study of flexible flapping wings by a coupled lattice Boltzmann-finite element approach with immersed boundary method," *Journal of Fluids and Structures*, vol. 49, pp. 516–533, 2014.
- ⁴¹B. Shrestha, S. N. Ahsan, and M. Aureli, "Experimental study of oscillating plates in viscous fluids: Qualitative and quantitative analysis of the flow physics and hydrodynamic forces," *Physics of Fluids*, vol. 30, no. 1, p. 013102, 2018.
- ⁴²A. N. Nuriev, A. M. Kamalutdinov, and A. G. Egorov, "A numerical investigation of fluid flows induced by the oscillations of thin plates and evaluation of the associated hydrodynamic forces," *Journal of Fluid Mechanics*, vol. 874, pp. 1057–1095, 2019.
- ⁴³M. Aureli, M. E. Basaran, and M. Porfiri, "Nonlinear finite amplitude vibrations of sharpedged beams in viscous fluids," *Journal of Sound and Vibration*, vol. 331, no. 7, pp. 1624–1654, 2012.
- ⁴⁴M. Aureli, C. Pagano, and M. Porfiri, "Nonlinear finite amplitude torsional vibrations of cantilevers in viscous fluids," *Journal of Applied Physics*, vol. 111, no. 12, p. 124915, 2012.
- ⁴⁵A. Tafuni and I. Sahin, "Non-linear hydrodynamics of thin laminae undergoing large harmonic oscillations in a viscous fluid," *Journal of Fluids and Structures*, vol. 52, pp. 101–117, 2015.
- ⁴⁶J. M. R. Graham, "The forces on sharp-edged cylinders in oscillatory flow at low Keulegan-Carpenter numbers," *Journal of Fluid Mechanics*, vol. 97, no. 2, pp. 331–346, 1980.

PLEASE CITE THIS ARTICLE AS DOI: 10.1063/5.0141889

⁴⁷P. W. Bearman, M. J. Downie, J. M. R. Graham, and E. D. Obasaju, "Forces on cylinders in viscous oscillatory flow at low Keulegan-Carpenter numbers," *Journal of Fluid Mechanics*, vol. 154, pp. 337–356, 1985.

- ⁴⁸S. N. Ahsan and M. Aureli, "Nonlinear oscillations of shape-morphing submerged structures: Control of hydrodynamic forces and power dissipation via active flexibility," *Journal of Fluids and Structures*, vol. 74, pp. 35–52, 2017.
- ⁴⁹S. N. Ahsan and M. Aureli, "Three-dimensional analysis of hydrodynamic forces and power dissipation in shape-morphing cantilevers oscillating in viscous fluids," *International Jour*nal of Mechanical Sciences, vol. 149, pp. 436–451, 2018.
- ⁵⁰L. Tao and K. Thiagarajan, "Low KC flow regimes of oscillating sharp edges I. Vortex shedding observation," Applied Ocean Research, vol. 25, no. 1, pp. 21–35, 2003.
- ⁵¹D. R. Brumley, M. Willcox, and J. E. Sader, "Oscillation of cylinders of rectangular cross section immersed in fluid," *Physics of Fluids*, vol. 22, no. 5, p. 052001, 2010.
- ⁵²C. N. Phan, M. Aureli, and M. Porfiri, "Finite amplitude vibrations of cantilevers of rectangular cross sections in viscous fluids," *Journal of Fluids and Structures*, vol. 40, pp. 52–69, 2013.
- ⁵³C. Conway, N. Jeffers, A. Agarwal, and J. Punch, "Influence of thickness on the flow field generated by an oscillating cantilever beam," *Experiments in Fluids*, vol. 61, p. 167, 2020.
- ⁵⁴S. N. Ahsan and M. Aureli, "Finite amplitude oscillations of flanged laminas in viscous flows: Vortex-structure interactions for hydrodynamic damping control," *Journal of Fluids and Structures*, vol. 59, pp. 297–315, 2015.
- ⁵⁵Y. Nakamura and M. Nakashima, "Vortex excitation of prisms with elongated rectangular, H and ⊢ cross-sections," *Journal of Fluid Mechanics*, vol. 163, pp. 149–169, 1986.
- ⁵⁶G. Schewe, "Nonlinear flow-induced resonances of an H-shaped section," *Journal of Fluids and Structures*, vol. 3, pp. 327–348, 1989.
- ⁵⁷Y. Kubo and K. Hirata, "Aerodynamic responses and pressure function of shallow H-section cylinder," *Journal of Wind Engineering and Industrial Aerodynamics*, vol. 33, no. 1-2, pp. 123–130, 1990.
- ⁵⁸T. Nakagawa and R. Nakagawa, "Vortex shedding mechanism from prisms having H and I sections," *Journal of Wind Engineering and Industrial Aerodynamics*, vol. 49, no. 1-3, pp. 197–206, 1993.

PLEASE CITE THIS ARTICLE AS DOI: 10.1063/5.0141889

This is the author's peer reviewed, accepted manuscript. However, the online version of record will be different from this version once it has been copyedited and typeset.

- ⁵⁹R. F. Schmit, M. N. Glauser, and G. Ahmadi, "Flow and turbulence conditions in the wake of a H-section in cross flow," *Journal of Fluids and Structures*, vol. 19, no. 2, pp. 193–207, 2004.
- ⁶⁰L. D. Landau and E. M. Lifshitz, "Fluid mechanics," Course of Theoretical Physics, vol. 6, 1959
- ⁶¹H. Schlichting, Boundary layer theory. New York: McGraw-Hill, 1979.
- ⁶²H. Schlichting, "Berechnung ebener periodischer Grenzschichtströmungen (Calculation of plane periodic boundary layer streaming)," *Physikalische Zeitschrift*, vol. 33, pp. 327–335, 1932.
- ⁶³N. Riley, "Steady streaming," Annual review of fluid mechanics, vol. 33, pp. 43-65, 2001.
- ⁶⁴A. Nuriev and O. Zaitseva, "Analysis of the secondary stationary flow around an oscillating circular cylinder," *International Journal of Mechanical and Mechatronics Engineering*, vol. 8, no. 11, 2014.
- ⁶⁵A. N. Nuriev and A. G. Egorov, "Asymptotic investigation of hydrodynamic forces acting on an oscillating cylinder at finite streaming Reynolds numbers," *Lobachevskii Journal of Mathematics*, vol. 40, no. 6, pp. 794–801, 2019.
- ⁶⁶M. Le Provost and J. D. Eldredge, "Mean transport of inertial particles in viscous streaming flows," *Physical Review Fluids*, vol. 5, p. 054302, 2020.
- ⁶⁷H. An, L. Cheng, and M. Zhao, "Direct numerical simulation of oscillatory flow around a circular cylinder at low Keulegan-Carpenter number," *Journal of Fluid Mechanics*, vol. 666, pp. 77–103, 2011.
- ⁶⁸K. Chong, S. D. Kelly, S. Smith, and J. D. Eldredge, "Inertial particle trapping in viscous streaming," *Physics of Fluids*, vol. 25, no. 3, p. 033602, 2013.
- ⁶⁹A. Nuriev, A. Kamalutdinov, and O. Zaitseva, "Hydrodynamics around long vibrating beams," *Journal of Fluids and Structures*, vol. 101, p. 103203, 2021.
- ⁷⁰F. K. Chan, Y. Bhosale, T. Parthasarathy, and M. Gazzola, "Three-dimensional geometry and topology effects in viscous streaming," *Journal of Fluid Mechanics*, vol. 933, p. A53, 2022.
- ⁷¹T. Açıkalın, A. Raman, and S. V. Garimella, "Two-dimensional streaming flows induced by resonating, thin beams," *The Journal of the Acoustical Society of America*, vol. 114, no. 4, pp. 1785–1795, 2003.

This is the author's peer reviewed, accepted manuscript. However, the online version of record will be different from this version once it has been copyedited and typeset. PLEASE CITE THIS ARTICLE AS DOI: 10.1063/5.0141889

- ⁷²C. W. Kotas, M. Yoda, and P. H. Rogers, "Visualization of steady streaming near oscillating spheroids," *Experiments in Fluids*, vol. 42, no. b, pp. 111–121, 2007.
- ⁷³S. A. Bahrani, N. Périnet, M. Costalonga, L. Royon, and P. Brunet, "Vortex elongation in outer streaming flows," *Experiments in Fluids*, vol. 61, no. 91, 2020.
- ⁷⁴J. T. Stuart, "Double boundary layers in oscillatory viscous flow," *Journal of Fluid Mechanics*, vol. 24, no. 04, pp. 673–687, 1966.
- ⁷⁵F. Noca, D. Shiels, and D. Jeon, "A comparison of methods for evaluating time-dependent fluid dynamic forces on bodies, using only velocity fields and their derivatives," *Journal of Fluids and Structures*, vol. 13, no. 5, pp. 551–578, 1999.
- 76 T. Sarpkaya, "On the parameter $\beta = \text{Re/KC} = D^2/\nu T$," Journal of Fluids and Structures, vol. 21, no. 4, pp. 435–440, 2005.
- ⁷⁷W. H. Chu, "Technical report no. 2," tech. rep., 1963.
- ⁷⁸J. R. Elston, J. Sheridan, and H. M. Blackburn, "Two-dimensional Floquet stability analysis of the flow produced by an oscillating circular cylinder in quiescent fluid," *European Journal of Mechanics B/Fluids*, vol. 23, no. 1, pp. 99–106, 2004.
- ⁷⁹X. Zhang, S. Ni, S. Wang, and G. He, "Effects of geometric shape on the hydrodynamics of a self-propelled flapping foil," *Physics of Fluids*, vol. 21, no. 10, p. 103302, 2009.
- ⁸⁰N. Arora, A. Gupta, S. Sanghi, H. Aono, and W. Shyy, "Flow patterns and efficiency-power characteristics of a self-propelled, heaving rigid flat plate," *Journal of Fluids and Structures*, vol. 66, pp. 517–542, 2016.
- ⁸¹S. Alben and M. Shelley, "Coherent locomotion as an attracting state for a free flapping body," *Proceedings of the National Academy of Sciences of the United States of America*, vol. 102, no. 32, pp. 11163–11166, 2005.
- 82 J. R. Chaplin, "Hydrodynamic damping of a cylinder at $\beta\approx 10^6$," Journal of Fluids and Structures, vol. 14, no. 8, pp. 1101–1117, 2000.
- ⁸³T. Sarpkaya, "Experiments on the stability of sinusoidal flow over a circular cylinder," Journal of Fluid Mechanics, vol. 457, pp. 157–180, 2002.
- ⁸⁴P. Hall, "On the stability of the unsteady boundary layer on a cylinder oscillating transversely in a viscous fluid," *Journal of Fluid Mechanics*, vol. 146, pp. 347–367, 1984.
- ⁸⁵F. Noca, On the evaluation of time-dependent fluid-dynamic forces on bluff bodies. PhD thesis, California Institute of Technology, 1997.

PLEASE CITE THIS ARTICLE AS DOI: 10.1063/5.0141889

Accepted to Phys. Fluids 10.1063/5.0141889

⁸⁶G. Falcucci, M. Aureli, S. Ubertini, and M. Porfiri, "Transverse harmonic oscillations of laminae in viscous fluids: a lattice Boltzmann study," *Philosophical Transactions of the Royal Society of London A: Mathematical, Physical and Engineering Sciences*, vol. 369, pp. 2456–2466, 2011.

⁸⁷M. Van Dyke, An album of fluid motion. Stanford, CA: Parabolic Press, 1982.

⁸⁸C.-Y. Wang, "On high-frequency oscillatory viscous flows," *Journal of Fluid Mechanics*, vol. 32, no. 1, pp. 55–68, 1968.

⁸⁹H. An, L. Cheng, and M. Zhao, "Steady streaming around a circular cylinder in an oscillatory flow," *Ocean Engineering*, vol. 36, no. 14, pp. 1089–1097, 2009.